



University of Tennessee, Knoxville
**Trace: Tennessee Research and Creative
Exchange**

Masters Theses

Graduate School

8-2008

Fusion Reaction Cross-section Measurements near ^{100}Sn

Elton Lewis Freeman

University of Tennessee, Knoxville

Recommended Citation

Freeman, Elton Lewis, "Fusion Reaction Cross-section Measurements near ^{100}Sn . " Master's Thesis, University of Tennessee, 2008.
https://trace.tennessee.edu/utk_gradthes/3636

This Thesis is brought to you for free and open access by the Graduate School at Trace: Tennessee Research and Creative Exchange. It has been accepted for inclusion in Masters Theses by an authorized administrator of Trace: Tennessee Research and Creative Exchange. For more information, please contact trace@utk.edu.

To the Graduate Council:

I am submitting herewith a thesis written by Elton Lewis Freeman entitled "Fusion Reaction Cross-section Measurements near ^{100}Sn ." I have examined the final electronic copy of this thesis for form and content and recommend that it be accepted in partial fulfillment of the requirements for the degree of Master of Science, with a major in Physics.

Robert Grzywacz, Major Professor

We have read this thesis and recommend its acceptance:

Carol Bingham, Lawrence Townsend

Accepted for the Council:

Dixie L. Thompson

Vice Provost and Dean of the Graduate School

(Original signatures are on file with official student records.)

To the Graduate Council:

I am submitting here-with a thesis written by Elton Lewis Freeman entitled “Fusion Reaction Cross-section Measurements near ^{100}Sn .” I have examined the final electronic copy of this thesis for form and content and recommend that it be accepted in partial fulfillment of the requirements for the degree of Masters of Science, with a major in Physics.

Robert Grzywacz
Robert Grzywacz, Major Professor

We have read this thesis
and recommend its acceptance:

Carrol Bingham

Lawrence Townsend

Accepted for the Council:

Carolyn Hodges
Carolyn Hodges, Vice Provost and Dean
of the Graduate School

(Original signatures are on file with official student records.)

Fusion Reaction Cross-section Measurements near ^{100}Sn

A Thesis Presented for
The Master of Science
Degree
The University of Tennessee, Knoxville

Elton Lewis Freeman
August 2008

Acknowledgments

I am exceptionally grateful to my thesis advisor Dr. Robert Grzywacz, who is always available to me for questions and answers in all aspects of the experiment. Even in some of the questions that I have pondered on he always finds a solution and explains in a way that related to the experiment and in which that I can understand it. Either if it is experimental or theoretical in nature it seems that he can always find information that concerns the experiment or for a class that I may be taking at the time. I have learned a lot from Robert on the aspects of experimental nature, it is like doing statistical mechanics, you make a prediction about what you expect to see and then you just do the experiment. I am indebted to him for his guidance, professionalism, and patience in helping me to understand this experiment.

For any graduate student, not matter what field of study, a graduate student learns more from their advisor than any other professor they will ever encounter. The details of writing publications, analyzing data, new technologies in experimental setups, and the experiment itself are some to the things to master.

In addition, I would also like to thank my other committee members for their inputs on this thesis and for being willing to serve on my thesis committee: Dr. Carol Bingham's nuclear physics course (Phys 341) was fun and appealing to physics as well as to the nuclear engineers who take his course. I have really enjoyed sitting in on his class lectures; he really seems to clarify things from when I first taken nuclear physics from undergrad. It is great to have a professor like Carol here at UTK, his favorite color is orange, a true UT fan.

Dr. Townsend's input is also greatly appreciated, since I will also have a minor in the field of nuclear engineering, I can get more input from the field of nuclear engineering aspects of the dynamics of the reactions.

Abstract

This thesis describes the measurement of production rates of $A=109$ isobars produced with beams of ^{54}Fe ions accelerated to 207 MeV bombarding ^{58}Ni target. The reaction products have been electromagnetically separated according to their mass over charge ratio and implanted into a semiconductor detector. The spontaneous decay radiation from the implanted radioactive isobars has been measured in a detection system with known detection efficiency, enabling to determine absolute intensities of observed isotopes. Known branching ratios of alpha decays of ^{109}Xe , ^{109}Te , proton decay of ^{109}I and beta delayed gamma radiation of ^{109}Te and ^{109}Sb have been used to determine the production rates of these isotopes. The experimental data has been compared to predictions given by the fusion-evaporation code HIVAP. The experiment was performed at Holifield Radioactive Ion Beam Facility at Oak Ridge National Laboratory using the 25 MV Tandem Accelerator and Recoil Mass Spectrometer. This work can be used in planning of future experiments on exotic isotopes near ^{100}Sn . Results for the production of ^{109}Sb were found to agree fairly well with HIVAP prediction, but should only be used as a guide for future experiments.

Table of Contents:

Chapter 1:	General Introduction	1
Chapter 2:	Decay Modes of Nuclei Near ^{100}Sn	7
2.1	Alpha, Beta, and Proton Decay.....	7
2.2	β^+ Decay Modes.....	7
Chapter 3:	The Experimental Apparatus.....	15
3.1	Heavy Ion Acceleration in Electrostatic Tandem	15
3.2	Rotating Target Assembly	17
3.3	Recoil Mass Spectrometer	22
Chapter 4:	Fusion Evaporation Cross-Section	29
4.1	Introduction to HIVAP Production Code	29
4.2	HIVAP and Apparatus Tuning	32
Chapter 5:	Detector Apparatus.....	37
5.1	Calibrating a Germanium (Gamma Detector)	37
5.2	Alpha Counts from Silicon Detector	40
Bibliography:	50

Chapter 1: General Introduction

Several experiments in the vicinity of the double-closed shell of $N=Z=50$ have concluded that alpha and proton emitters exist in a small island near ^{100}Sn . In this region the heaviest $N=Z$ nuclei reach the proton drip line. This existence of the alpha emission island provides an opportunity for studies of the structure of nuclei far from stability. Nuclear decay modes represented in this region are alpha, proton and β^+ decay.

Figure 1, shows a recent representation of the nuclear chart. The vertical axis represents the proton number and the horizontal axis being the neutron number. In the center of the chart, black squares represent nuclei that are stable and this valley is called the line of stability. Above the line of stability, is where nuclei will decay by β^+ transformation, this area is colored red along the chart. Nuclei below the line of stability are nuclei that may decay by β^- transformation and these nuclei are represented on the chart as blue squares. The squares marked in yellow represent the nuclei that are known to decay by alpha decay. Observing the chart, most heavy nuclei in the vicinity around $N=Z=82$ decay by alpha emission, and a close look around $N=Z=50$ reveals a small island of nuclei of medium mass that also decay by alpha decay; in the remainder of this thesis this island will be designated as Alpha Island.

The green squares represent those nuclei that decay by spontaneous fission where the parent nucleus splits into two smaller nuclei. This reaction process is accompanied by the ejection of one or more neutrons. It has been known that some heavy nuclides with $A>230$ will decay via spontaneous fission.

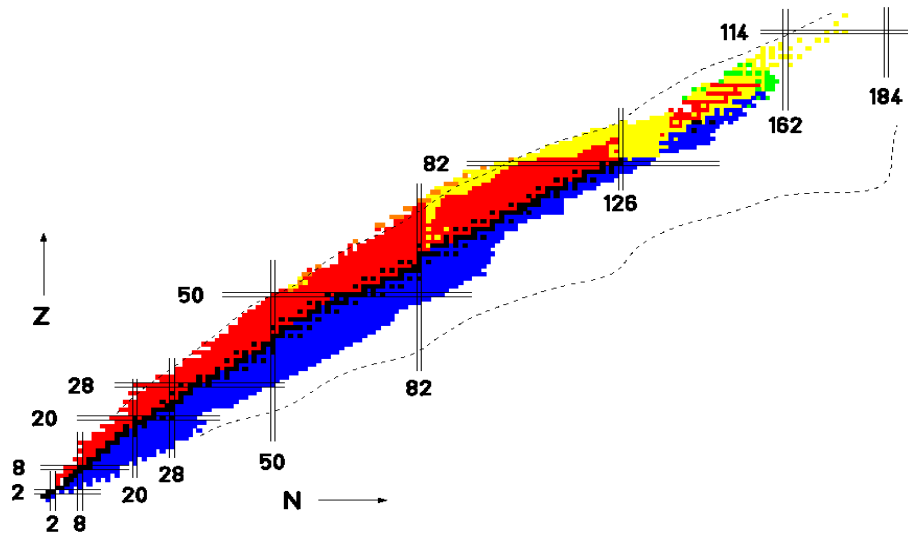


Figure 1: Picture of the nuclear chart showing the transformation mechanisms of β^+ as red squares, β^- as blue, and alpha decay as yellow squares, and green as spontaneous fission. A small island of alpha decay is measured to exist above ^{100}Sn . [1]

Production of nuclei far from stability requires the use of accelerator facilities.

This is made complicated by the fact that the production cross-sections drop off rapidly when departing from the valley of stability (black squares in figure 1). Several accelerator facilities have been constructed to produce these nuclei. Some examples in the United States are Holifield Radioactive Ion Beam Facility (HRIBF) at Oak Ridge National Laboratory, Atlas Facility at Argonne National Laboratory, National Superconducting Cyclotron Laboratory (NSCL) at Michigan State University, and the 88 inch Cyclotron at Lawrence Berkeley National Laboratory (LBL).

The Holifield Radioactive Ion Beam Facility (HRIBF) accelerates beams of stable or radioactive ions with a folded tandem accelerator. The tandem accelerator utilizes a pelletron to produce a high accelerating voltage. The tandem operates at voltages up to

25 million volts. Negative charged ions entering the base of the tandem tower are accelerated up to the hollow conductor terminal where the tandem has the greatest potential. Once the ions reach the high voltage terminal, they bombard a stripper foil which removes electrons giving these ions a positive charge. These ions are deflected through 180° with a magnetic dipole magnet in the high-voltage terminal and are accelerated back to ground potential.

The Atlas Facility uses a superconducting linear accelerator. The method of accelerating charged ions uses radio-frequency controlled electric fields generated through resonators, as if the accelerating wave is propagating through the accelerator. The charged ions are injected just before the electric field is created and these ions ride along with the accelerated electric field to the target.

The National Superconducting Cyclotron Laboratory at Michigan State University uses circular accelerators. The performance of these circular accelerators is based on the highest magnetic rigidity of ions they can accelerate. K500 & K1200 coupled cyclotrons are different in construction from the two linear accelerators discussed above. Instead of using a linear drift tube, these accelerators are circular. They can continuously re-accelerate beams making them more compact. Cyclotrons use electric potential to accelerate ions and they also use magnetic fields to keep these ions in a circular orbit. Heavy ions can be accelerated to energies of more than 100 MeV/A at the NSCL. This facility focuses on producing beams of nuclei using the fragmentation reactions.

The 88-inch K-140 cyclotron at LBL is similar to the K500 & K1200, but to accelerate ions to energies of only 4.5 MeV/A with a radio-frequency potential. Studies at the Berkeley Laboratory include nuclear structure as well as heavy element studies.

For the research discussed in this thesis HRIBF was used to accelerate heavy ion beams of stable isotopes with high intensity and quality to energies of a few MeV per nucleon. The stable isotope beams bombarded a stable isotope target inducing fusion evaporation reactions. A Recoil Mass Spectrometer (RMS) was used to separate reaction products according to their A/Q ratios. A sophisticated detection system measured the decay properties of specific nuclei. The uniqueness of HRIBF lies in the fact, that it can also accelerate radioactive beams produced by proton induced fission of ^{238}U . The proton beams of 50 MeV energy are delivered by Oak Ridge Isochronous Cyclotron (ORIC).

Currently the focus of nuclear structure studies is on nuclei very far from beta stability, because of the interest in understanding the variation of nuclear properties as a function of drastic changes of proton and neutron number. One challenge in studies of exotic nuclei is in their production in nuclear reactions with rapidly diminishing cross-sections. Limited production rates makes gamma spectroscopy more complicated due to the difficulty of finding photo-peaks in relation to background counts.

The focus of this thesis is on studies of nuclei near the double magic nucleus ^{100}Sn , which has closed shells for both neutrons and protons. The main question presented in this thesis is how does the production cross-section of nuclei change with changes in proton and neutron binding energies?

The nuclear binding energies of isotopes in this region have an astrophysical context. It is predicted [1] that the process of nucleosynthesis along the proton drip line, the so called rp-process, terminates in this region of the nuclear chart with a SnSbTe cycle. The presence of this cycle SnSbTe depends on nuclear properties, like lifetimes, binding energies of isotopes, and Q values for proton and alpha emission in this region. Today the rp-process is thought to end at Alpha Island near ^{100}Sn due to the alpha and proton instability of nuclei in this region. In the island of alpha decay, a proton capture to Sn and Sb is possible, but a proton capture to Te will be followed by absorption of a gamma ray (photo disintegration) and alpha particle emission, which resets the cycle each time tellurium isotopes are reached by the rp-process.

Studies have concluded that the $N=Z$ effects create an enhanced alpha decay, the so called super allowed alpha decay [2,3]. Nucleons, that occupy the same single particle orbital, in this case $1g_{7/2}$ or $2d_{5/2}$ may experience pairing forces between the valence neutrons and protons around the closed $N=Z=50$ shell. Such pairing forces may enhance the alpha pre-formation factor (P_α), or a probability that the alpha particle can be formed inside the nucleus and tunnel through the Coulomb barrier to escape.

The main goal of this research was to determine the production cross-section of ^{109}Te , ^{109}I , ^{109}Xe , ^{109}Sb ions that are produced in collisions of 207 MeV primary beams of ^{54}Fe ions bombarding a ^{58}Ni target. The compound nucleus produced in this reaction ^{112}Xe will evaporate protons, alphas and neutrons leading to production of lighter nuclides of xenon, iodine, tellurium, and antimony. Among the evaporation products are both proton and alpha emitters, which can be measured with very high efficiency with the

charged particle detectors. From the number of counts (detected alpha decays), the total number of recoil products reaching the focal plane of the RMS can be estimated. The absolute production rates can be approximated since the transmission of the ions through the Recoil Mass Spectrometer (RMS) is estimated as 5% [4]. The measured production cross-sections will be compared to theoretical predictions of the fusion-evaporation code HIVAP.

Chapter 2: Decay Modes of Nuclei Near ^{100}Sn

2.1 Alpha, Beta, and Proton Decay

Positron beta decay (β^+) involves the transformation process in which a proton in the nucleus turns into a neutron, emitting a positron and a neutrino. The positron and the neutrino both fly out of the nucleus leaving it with one less proton and one more neutron. Since the atomic number (Z) changes, this is one way of transforming elements. For example, tellurium positron decay results in antimony. In the transformation process, the number of neutrons (N) and protons (Z) will change, but the total mass number (A) of the nuclide will remain unchanged.

2.2 β^+ Decay Modes

Electron capture competes with β^+ emission in nuclides with excess protons. Proton rich nuclei can capture an electron, usually in the lowest orbital, the K-shell, and the captured electron is used to convert a proton into a neutron. This decay process increases the number of neutrons making the resulting nucleus closer to the line of stability. A nearby electron will then fill in the empty K-orbital and will emit a characteristic X-ray of 20-30 keV (in the Sn region), verified in the gamma detector spectroscopy of this experiment. The process will result in the change of the element, e.g. tellurium will become antimony.

Among beta decaying isotopes in this region, there are confirmed beta delayed proton emitters such as $^{109}\text{Te} \rightarrow ^{109}\text{Sb} + \beta^+ \rightarrow ^{108}\text{Sn} + \text{p}$ (branching ratio 9.40%) and beta delayed alpha emitters, like $^{109}\text{Te} \rightarrow \beta^+ + ^{109}\text{Sb} \rightarrow ^{105}\text{In} + \alpha$, with the beta delayed alpha

emission branch $\sim 5.0 \times 10^{-3} \%$. Tellurium represents a good example of competition between all decay processes, that of alpha, proton, beta emission, and electron capture and making it a good candidate for detection with charged particle detectors.

Beta delayed proton decay has been observed in Alpha Island. Figure 2 shows a magnified view of an Alpha Island, the nuclei of interest here are ^{109}Te and ^{109}Sb . This process takes two steps. The mother nucleus (^{109}Te) will decay by emitting a β^+ particle and populates excited states in the daughter (^{109}Sb). The condition for beta-delayed proton decay is possible if levels populated in the daughter have energy greater than the binding energy of the proton. It would then be energetically favored to decay by proton emission in comparison to gamma emission. ^{109}Te is a good example of a nucleus with this type of decay mode, as well as other modes discussed.

One the most common decay modes is, beta delayed gamma emission. In order for this process to happen, the β^+ decay from the mother nucleus will populate excited states in the daughter nucleus with energies below or slightly above the proton separation energy. The gamma rays typically have a few hundred keV.

Both alpha and proton decay modes are found in the vicinity of ^{100}Sn . The mechanism by which the alpha particles form within the nucleus is not known exactly. After formation, the alpha particle will have to tunnel through the Coulomb barrier in order to escape from the nucleus. It is modeled like a particle in a potential well; where the particle has some energy as it bounces back and forth inside the barrier. A simple quantum mechanical model can be used to predict the probability of tunneling, which is related to the energy of the particle as it collides with the barrier, the barrier thickness and

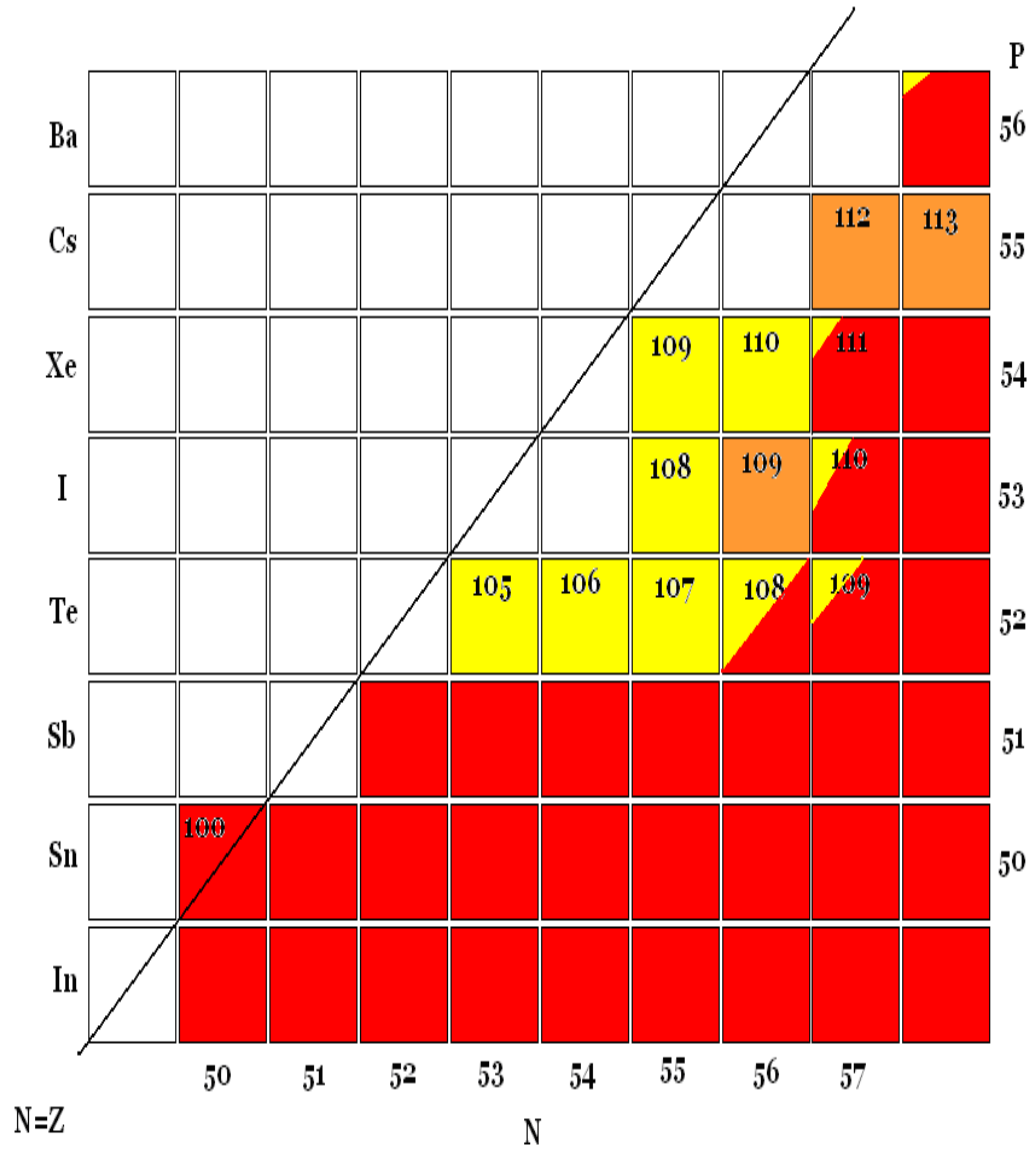


Figure 2: Magnified view of an Alpha Island, brown squares represent nuclei that proton decay, yellow presents those nuclei that alpha decay and red indicates those nuclei that decay by positron emission. Alpha emitting nuclei cluster around the $N=Z=50$ line that is drawn diagonal across the section of the chart.

the barrier height. Taller and thicker barriers will result in a reduced probability for alpha decay.

Proton decay is similar to alpha decay, in that both have to tunnel through a Coulomb barrier. Proton decay occurs beyond the proton drip line where the proton separation energy is negative, and resulting in leaking of protons out of the nucleus. Direct proton decay is observable in a few nuclei in the region of interest such as $^{112,113}\text{Cs}$ and ^{109}I . The proton decay is simpler than alpha decay because it does not require a pre-formation process.

The island of proton and alpha decay above the ^{100}Sn nucleus has been investigated in several experiments, [5], [2], [3] and more. The above mentioned decay modes important in this region are represented for $A=109$ nuclei in this work. ^{109}Te disintegrates predominately by beta decay and electron capture, (branching ratio of 96.10%), and alpha decay (branch of 3.9%). Other isotopes such as ^{109}I and ^{113}Cs are proton emitters. Recently, Mazzocchi et al. [5] found an alpha decay branch in ^{109}I , with a branching ratio of $(1.4 \pm 0.4) \times 10^{-4}\%$. ^{109}Sb decays by $\beta^+/\epsilon\text{c}$ emission with a 100% branching ratio, and no other decay modes have been proposed for these nuclei.

The decay modes of ^{109}Te are shown in figure 3, in this example beta decay of ^{109}Te populates excited discrete and continuum states of ^{109}Sb . When the resulting ^{109}Sb has excitation energy above the proton separation energy of about 2.4 MeV, proton decay will be energetically favorable. The measured branching ratio for beta-delayed proton emission is 9.40% of the $\beta/\epsilon\text{c}$ for this nucleus.

When the nucleus ^{109}Te decays by β^+ to excited states below 2.4 MeV, gamma rays will be emitted from the resulting daughter nucleus, ^{109}Sb . The beta delayed proton emission that occurs with a branch of 9.40% and results in a nucleus of ^{108}Sn in either the 0^+ ground state or the first excited 2^+ state.

The odd mass isotopes ^{109}I and ^{113}Cs and even mass nuclide ^{112}Cs are proton emitters. Table 1 contains a list of all the charged particle decays of tellurium along with the branching ratios, which are normalized to unity. The implantation rate on the DSSD had to be maximized in order to observe data from nuclides with small production cross-sections and decay by particle emission that is a small fraction of the total decays.

2.3 Previous Studies of Tellurium Nuclei.

The studies of nuclei in the Alpha Island region (figure 2) date back to the 1960s when the fusion-evaporation reaction enabled by the construction of heavy-ion accelerators was exploited extensively to study nuclei far from stability, such as the neutron-deficient trans-tin isotopes which represent the complex decay behavior of beta, electron capture, alpha decay, beta delayed proton and alpha emissions. These exotic decays can be observed only by selective detection techniques. By improving techniques many recent experiments have used charged particle decays as a means of finding much needed information like half-life and nuclear structure.

In one of the earliest studies in the ^{100}Sn region, alpha decays from two tellurium isotopes of $^{107,108}\text{Te}$ were observed by R.D. Mac Farlane & Siivola [3]. They used ^{96}Ru projectile ions of 95 MeV to bombard a ^{16}O target, resulting in production of ^{108}Te by a 4 neutron evaporation channel. They observed two alphas one at 3.08 MeV suggested to

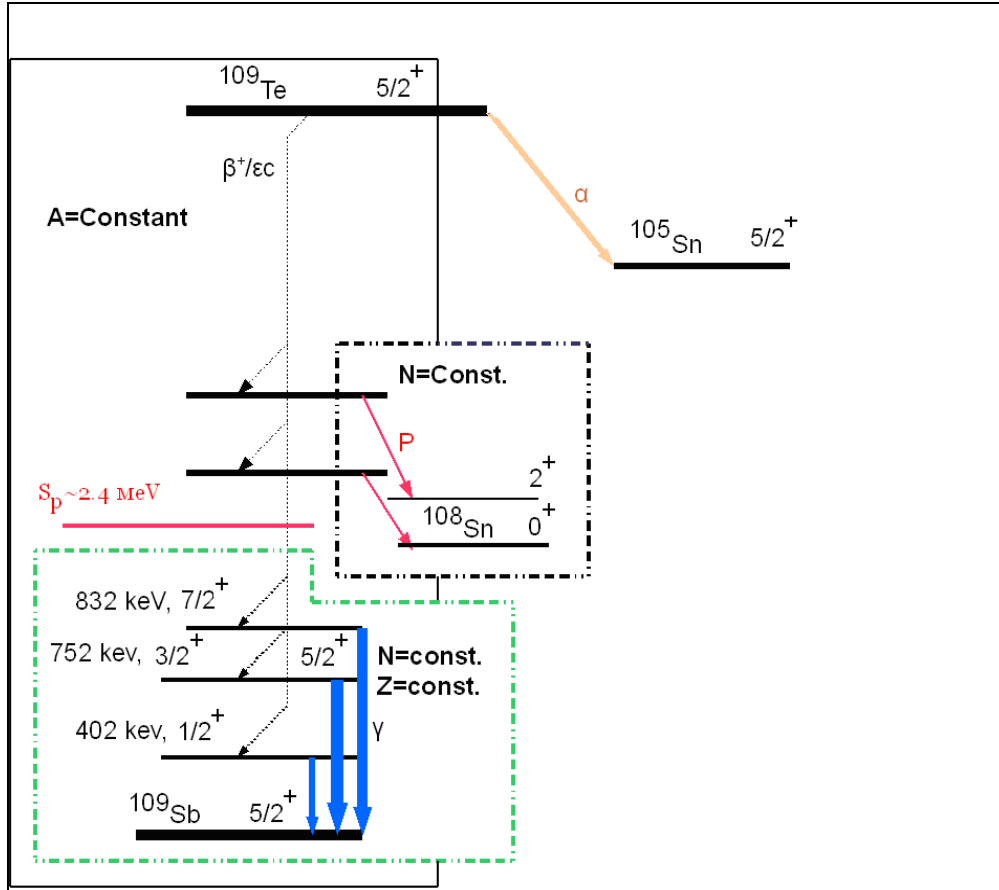


Figure 3; Schematic diagram showing the decay types for ^{109}Te of which gammas listed are the most intense peaks. The process of beta-delayed proton emission is given if states are populated above the proton binding energy of 2.4 MeV. An example of alpha decay is given above, where ^{109}Te decays to ^{105}Sn by emitting an alpha particle.

Table 1: ^{109}Te branching ratios for beta and alpha decays with the rare occurrence of beta delayed alpha decay shown at bottom. Beta and electron capture both occur 96.10% and the beta delayed proton emission occurs for 9.40% of the $\beta^+/\epsilon\text{c}$ decays.

Charged Particle Decay	Relative Branching Ratio
Beta Decay, (Electron Capture)	96.10%
Beta Delayed Proton Emission	9.40%
Alpha Decay	3.90%
Beta Delayed Alpha Decay	$<5.0 \times 10^{-3}\%$

result from the decay of ^{108}Te and another at 3.28 MeV suggested belonging to the decay of ^{107}Te . The half-life of ^{108}Te was estimated to be 4.2 seconds.

In 1967, V.A. Karnaukhov et al. [6] published papers suggesting that the 3.08 MeV alphas belong to ^{109}Te in contradiction to the findings of Mac Farlane and Siivola. Production of ^{109}Te was accomplished by a 3 neutron evaporation channel $^{92,94}\text{Mo}(^{20}\text{Ne}, 3n)$. The half-life of ^{109}Te was found to be 4.2 seconds. Other papers also confirmed the half-life of ^{109}Te as 4.2 seconds with the 3.08 MeV alpha particle belonging to ^{109}Te .

In another experiment conducted by [7], Roeckl et al. used reactions of 290 MeV ^{58}Ni ions on ^{58}Ni targets to study isotopes in the Alpha Island [figure 2]. Isotopes of $^{107, 108, 109, 110}\text{Te}$, $^{110-113}\text{Xe}$, and ^{114}Cs were observed by Roeckl and his results confirmed that 3.08 MeV alpha particles resulted from decay of ^{109}Te as first observed by Karnaukhov.

Z. Dombradi et al. [8] found the first evidence of fine structure of ^{109}Te from an inverse reaction of ^{58}Ni at 270 MeV bombarding ^{54}Fe target (*opposite of this experiment*) from the 2 proton 1 neutron evaporation reaction. Excited states of the neutron deficient nucleus ^{109}Te were identified for the first time. The method of detection used an in-beam γ -spectroscopic method to identify these new levels. Before this experiment only the ground state energies were known, but this work resulted in a many new levels of tellurium including higher excited levels.

J. Ressler et al. [9], observed intense gamma ray transitions (402,752,831.6 keV) below the 2.4 MeV excitation energy in ^{109}Sb populated by beta + decay of ^{109}Te and level spins of $(1/2^+, 3/2^+, 5/2^+, 7/2^+)$ were deduced. The activity was produced with an

inverse reaction of 260 MeV ^{58}Ni bombarding a ^{54}Fe target (*opposite of this experiment*) producing ^{112}Xe , and production of ^{109}Te by a 1 neutron 2 proton evaporation channel.

Experiments from Oak Ridge National Laboratory performed by C. Mazzocchi et al [5] and S.N. Liddick et al [2] have shown evidence of proton and alpha decay in the vicinity of the double magic nucleus of tin. For example, ^{109}I was thought originally to be a 100% proton emitting nucleus; however, Mazzocchi and collaborators found a small branching ratio ($\sim 10^{-4}\%$) for alpha decay. The ^{109}I activity was produced by bombarding a ^{58}Ni target with ^{54}Fe (*inverse reaction, opposite to this experiment*) giving ^{109}I by means of the 1 proton 2 neutron evaporation channel.

S. N. Liddick et al. found new alpha emitters of ^{109}Xe and ^{105}Te as a result of multiple alpha emissions, $^{109}\text{Xe} \rightarrow ^{105}\text{Te} \rightarrow ^{101}\text{Sn}$. Two new alpha particles were associated with the α decay of ^{109}Xe and ^{105}Te . The ^{109}Xe activity was produced in the normal reaction $^{54}\text{Fe}(^{58}\text{Ni}, 3n)^{109}\text{Xe}$ (*similar to this experiment*) channel where the beam energy was set to 207MeV for maximizing ^{109}Xe .

In this experiment, production cross-section of isobars such as ^{109}Xe , ^{109}I , ^{109}Te , and ^{109}Sb by particle evaporation as a result of the normal kinematic reaction of ^{54}Fe at 207 MeV bombarding a ^{58}Ni target to produce an excited nucleus ^{112}Xe was measured. The production of these ions can be counted by observing charged alphas and protons, or by detecting gamma decays. These decay modes will be used to determine the production rate of products from the compound nucleus ^{112}Xe as produced by bombardment of a ^{58}Ni target with a 207 MeV ^{54}Fe beam. Finally a calculation of the cross-sections will then be used to compare with HIVAP data.

Chapter 3: The Experimental Apparatus

3.1 Heavy Ion Acceleration in Electrostatic Tandem

The electrostatic tandem accelerator is used to accelerate heavy ions at HRIBF (see figure 4). The tandem accelerator uses a high potential to accelerate charged ions to a few MeV per nucleon, the energetic ions are used to induce nuclear reactions, for example the fusion of the target and beam nuclei.

A technique to change the charge state of an atom can be accomplished by colliding singly ionized atoms to other atoms with relatively lower electron affinity. Once these two different atoms collide, electron exchange occurs and the singly ionized atoms (^{54}Fe) with $Q = +1$ charge becomes negatively charged which enables them to be accelerated by the positive potential of the tandem accelerator. Methods for production of stable beams to be injected into the tandem are similar to the concepts outlined above. The heavy ions are sputtered out of the solid state materials (99.9% enriched ^{54}Fe) via electron beam bombardment. Positive ions extracted from the ion source are guided to a cesium cell located inside the Injector for Stable Ion Species (ISIS of figure 4) that contains a cesium gas with a low electron affinity.

Negative ions emerging from the charge exchange cell were accelerated to several keV and directed towards the tandem accelerator with use of steering magnets. The negatively charged ions of iron are attracted to the positive terminal of the electrostatic tandem accelerator where the potential can be as high as 25 million volts. The energy gained by the negative ion is $E_1 = |q_1 V|$, where $q_1 = -1$ and V was the terminal

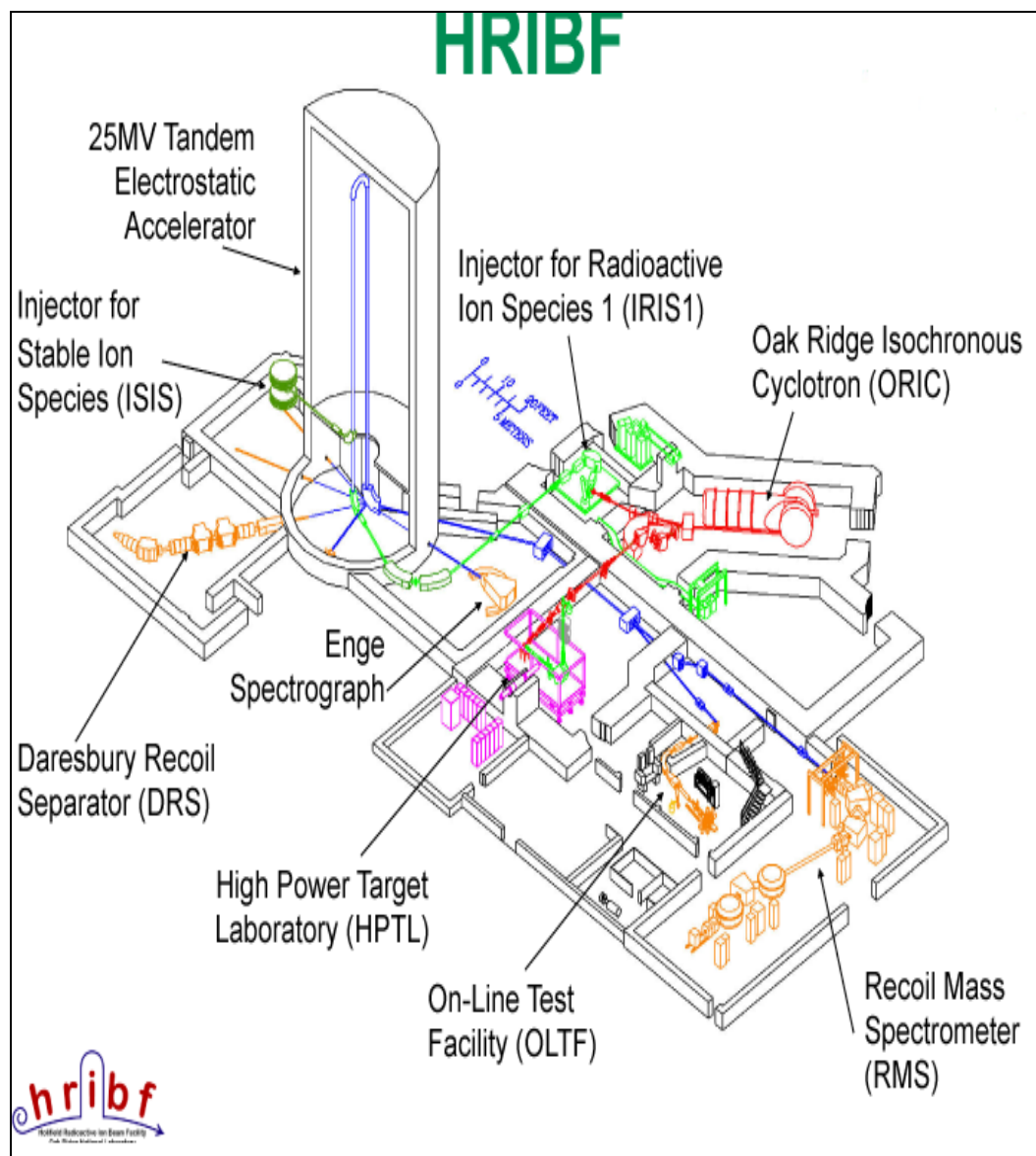


Figure 4: Floor plan of HRIBF showing the ISIS, Tandem Accelerator, and the RMS. The isotope ^{54}Fe was housed in the Injector for Stable Ion Species at upper left. Ions were extracted and sent to the tandem where they were accelerated and bending magnets directed them to the Recoil Mass Spectrometer where fusion evaporation reactions with the stable ^{58}Ni target occurred. Detectors at the focal plane of the RMS were used to detect the decay of the fusion evaporation nuclides.

voltage. The high voltage at the terminal of the tandem is generated by the pelletron(see figure 5, [9]). When the ions reach the top of the tandem, they pass through a stripper foil and lose several electrons. Multiply ionized atoms (positive charge) are repelled from the positive voltage of the terminal and gain energy on the way back to ground potential of $E_2=q_2V$. Thus, the total energy of an emerging ion is:

$$E_{\text{total}} = E_1 + E_2 = q_1V + q_2V = (1 + q_2)V \quad \text{Eqn. (1)}$$

V is electric potential of the tandem accelerator terminal. In order to accelerate emerging ions in +11 charge states to a beam energy of 207 MeV, the required terminal potential was:

$$V = 207 \text{ MeV} / (1 + 11) = 17.3 \text{ million volts} \quad \text{Eqn. (2)}$$

The projectile ions were then guided to the target station at the RMS (see figure 4).

3.2 Rotating Target Assembly

The projectile ions, or primary beam ions, with a kinetic energy of 207 MeV bombarded a target at the entrance of the Recoil Mass Spectrometer. Because high intensity beams are needed to maximize reaction yields, a rotating target assembly was implemented (see figure 6). In the experiment, the rotating target assembly was used to improve dissipation of heat caused by energy loss from the beam in the target. Energy loss effects may be due to collisions with electrons in the target material causing the target to heat up and glow. From the Stefan Boltzmann law, one can find the temperature of objects such as the target that may behave as a blackbody by using a correction factor or emissivity for non-ideal black body. If the power loss from the beam can be estimated,

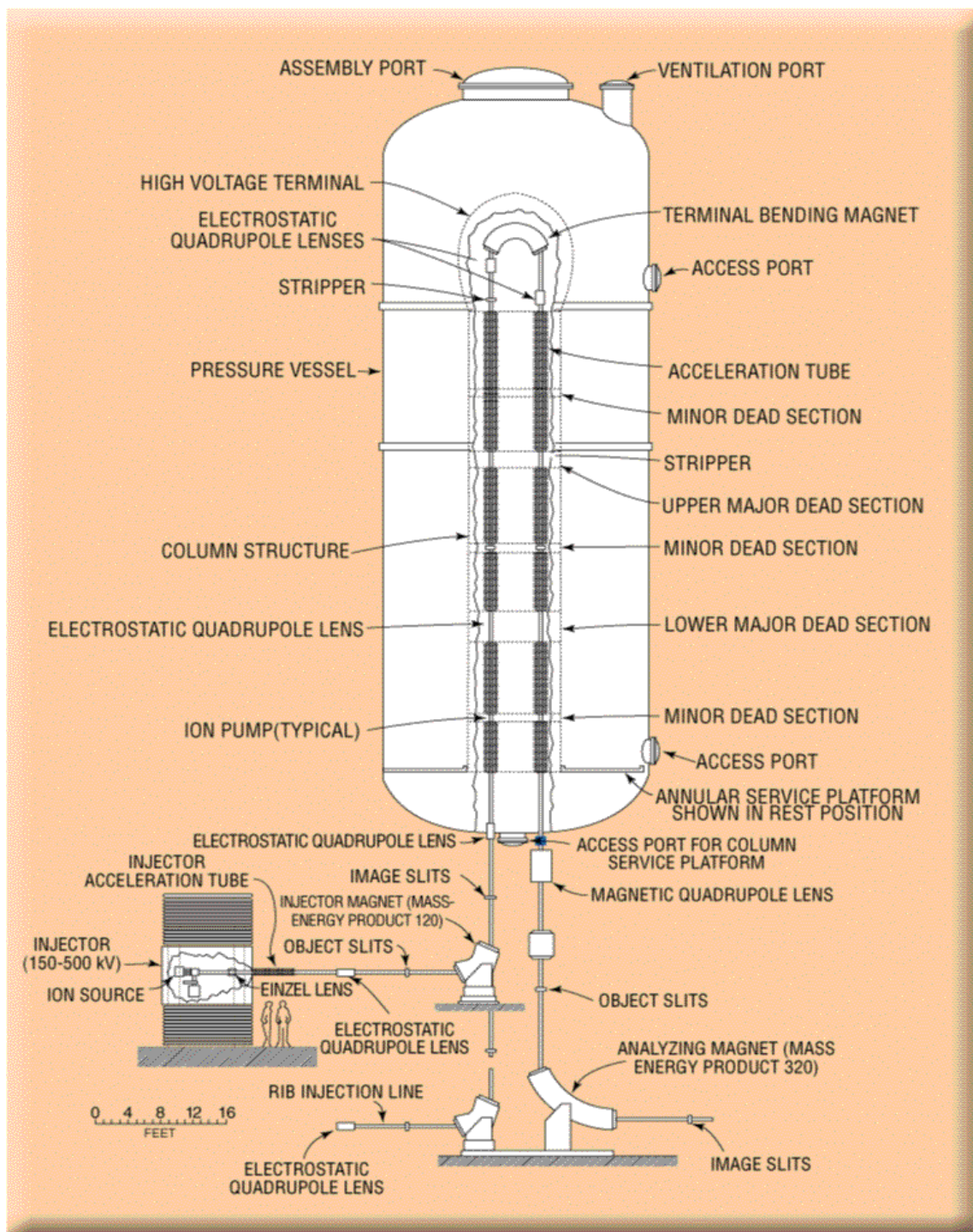


Figure 5: Schematic view of the tandem accelerator at HRIBF. A normal human height is given at the base (lower left hand side) for a scale. [10, 11]

one substitutes the power loss into P in equation 3 to find the temperature of the target. In order to estimate the temperature in the target, one would also have to model the heat flow through the crank mechanism, but this would be beyond the scope of this thesis, instead one can compare the power loss with the color of the target. An estimate of the temperature is made based on two methods, by the energy lost from the beam moving through the target and based on temperature. A comparison will be presented for both methods below.

During the experiment, it was observed that the target material was glowing red. According to the Stefan Boltzmann Law, the radiation emitted from the target can be estimated from equation 3. Variables in equation 3, are the area = A exposed on the front side and back side of target, this is the total area available to emit radiation, temperature of the target material = T, and the σ = Stefan Boltzmann constant.

$$P = \sigma A \epsilon T^4 \quad \text{Eqn(3)}$$

In order to estimate the temperature of the target, observation of the surface color of the target was observed as a red color and this color corresponds to a temperature of T ~1000K for a black body (see figure 6). The available area emitting radiation of the target would be the beam contact area in the front of the target and the same area on the back of the target. The back of the target must also be included since the back of the target is also glowing red (emitting electro-magnetic radiation). The area of the target on the front side and back was estimated from the diameter of the beam. The area for the rotating target assembly was estimated for a circular area swept by the beam (see figure 6). The emissivity of nickel can be estimated to be $\epsilon \sim 0.20$. If the temperature of the

target is higher than the melting point of nickel, then the incoming beam will melt a hole through the target.

In the center of figure 7, the nickel target is shown attached to a motor via a crank mechanism, similar to the design of a crankshaft; here it is used to convert the electric motors rotating shaft into a circular reciprocating motion of target. The circular motion dissipates heat across a large surface of the nickel target. The total power that can be dissipated is greater since the power loss is now spread out over a larger area. Increasing the area will then allow more heat to flow away from the hot spots of the target. With a beam current of 40 particle nano-amperes the beam spot attains an estimated temperature of 3100°C for a non-rotating target assembly and 730°C for the rotating target assembly. The higher temperature of 3100 C far exceeds the melting point of nickel (1455 C). With the beam focused on a circular spot of 0.25mm diameter as with the non-rotating target the Stefan Boltzmann Law predicts that the beam current would be limited to 3-5 pA in order to keep from melting the target.

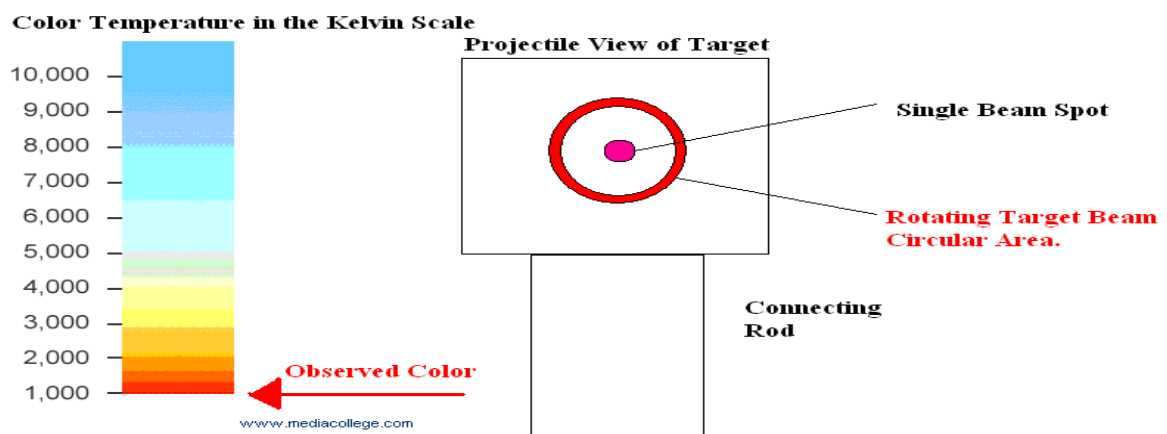


Figure 6: Color scale used to determine temperature for the radiating target.

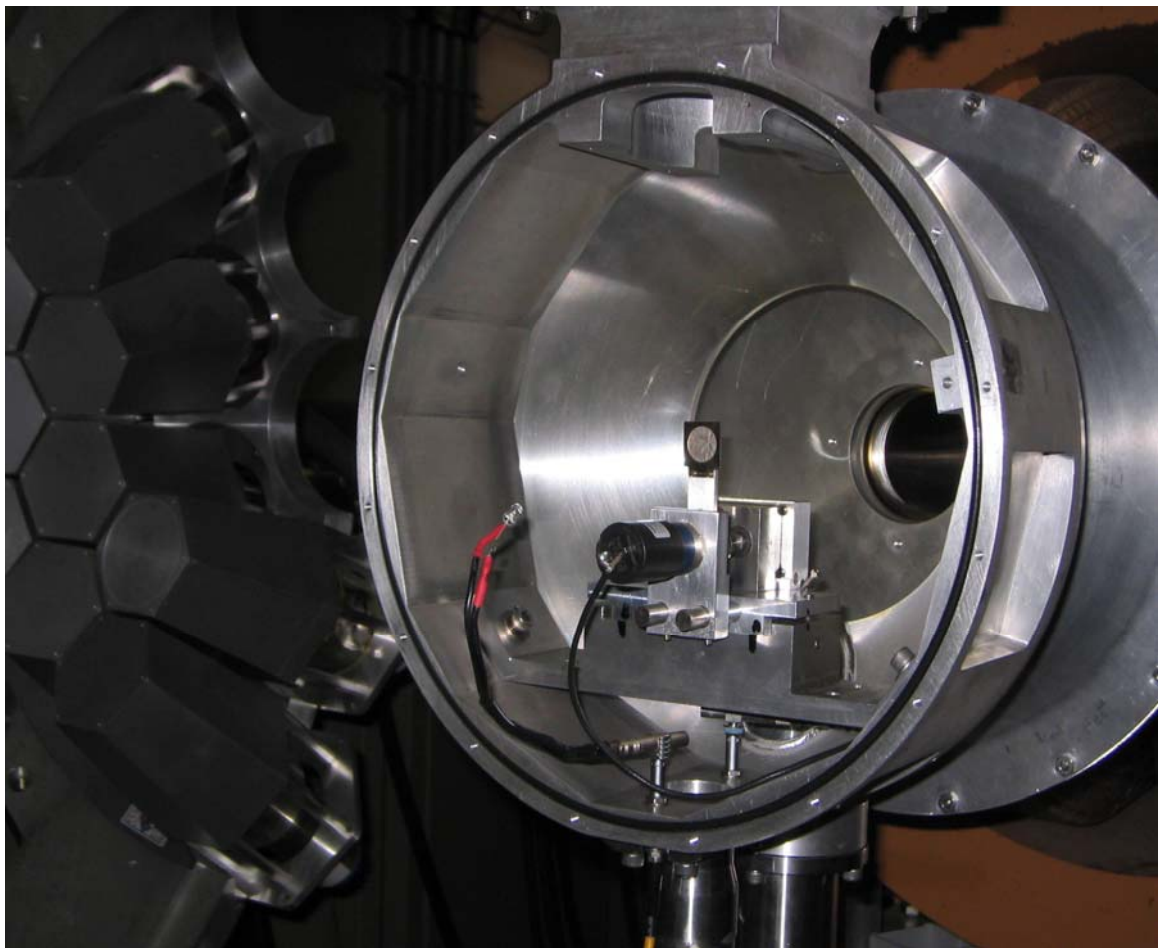


Figure 7; Rotating Target Assembly, outer layer is the target chamber, inside at the center a thin strip is where the target ^{58}Ni is located. Just below the target is the crank mechanism and the electric motor that turns the target by crankshaft.

3.3 *Recoil Mass Spectrometer*

The Recoil Mass Spectrometer (RMS) is a tool used to separate nuclei of different A/Q values for nuclear structure studies. The properties of the RMS such as primary beam suppression and a large angular and momentum acceptance give an efficiency that allows scientists to study nuclei farther from stability. As an example, this device has been used to study nuclei with production yields of less than 0.001% of the total cross-section [5]. The RMS has multiple magnetic and electrostatic components to separate ions based on mass to charge ratio. The RMS is divided into two sections, the first being the momentum separator and the second the mass separator, both are synchronized to maximize the transmission for the ions with the desired mass over charge (M/Q).

Ions are bent as they move through electric and magnetic fields due to their charge. This charge state of the ion is a result of collisions with electrons in the target and depends on the recoil velocity of the ions as they leave the target. Ions with A=109, result from the fusion reaction process and have a range of charge states and momentum.

Electric fields will accelerate positive ions in the direction of the field. The RMS uses an electrostatic dipole that creates an electric field similar to that of a parallel plate capacitor, but has curved plates to keep ions traveling along a uniform circular orbit.

Charged particles traveling perpendicular to a magnetic field experience a Lorentz Force perpendicular to both **v (velocity vector in bold)** and the **B** magnetic field (**vector in bold**) as:

$$\mathbf{F} = q\mathbf{v} \times \mathbf{B}. \quad \text{Eqn(4)}$$

The RMS consists of several magnetic and electrostatic components as shown in figure 8. There are three magnetic dipoles, labeled as D1, D2, and D3, that spatially separate ions based on their momentum. The Q's in figure 8 represent the focusing lenses or magnetic quadrupoles used to focus ions, the S's represent magnetic sextupoles and these are used to correct for imperfections in the design of the first magnetic dipole and first set of quadrupoles. The fingers were not needed for this experiment, and the ED's represent the electro-static dipoles that disperse in relation to energy. Ions with $A=109$, resulting from the fusion reaction process, have a range of charge states and momentum.

In the magnetic dipoles the magnetic fields and the ion velocities are perpendicular to each other and equation (4) reduces to $F=qvB$.

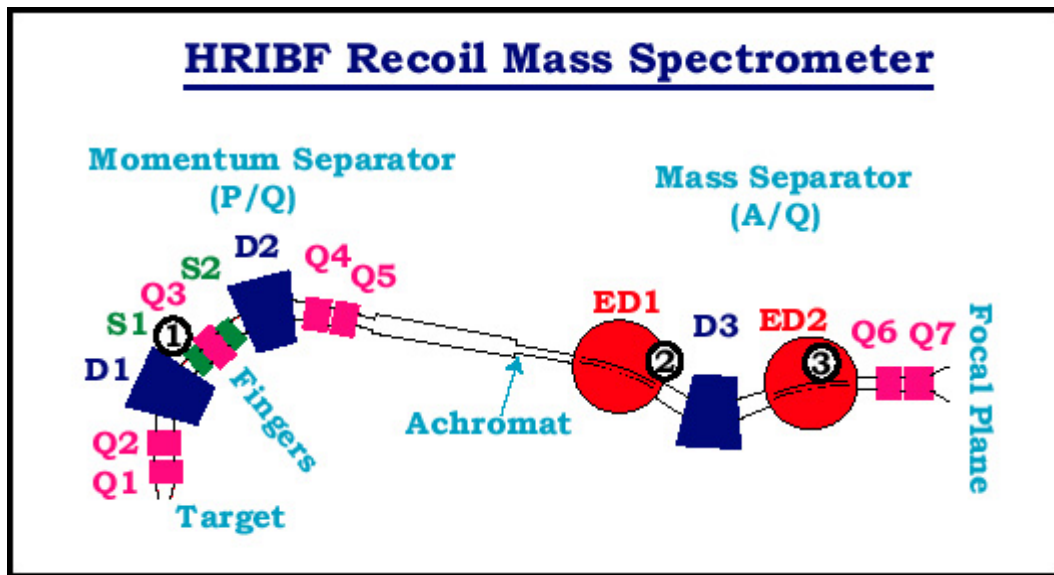


Figure 8: Recoil Mass Spectrometer showing all 14 components that separate ions based on A/Q . The RMS is divided into two sections, a momentum achromat (left) and a mass separator portion at right hand side[11]. Fingers were not needed for this experiment.

In the magnetic dipoles the magnetic fields and the ion velocities are perpendicular to each other and equation (4) reduces to $F=qvB$. Since the magnetic force is perpendicular to the velocity, it merely deflects the ions in a circular orbit of radius R_{MD} and by Newton's Law:

$$Q_0 v_0 B = (M_0 v_0^2) / R_{MD}$$

$$B = M_0 v_0 / Q_0 R_{MD} = p_0 / (Q_0 R_{MD}) = \frac{\sqrt{2M_0 E_0}}{Q_0 R_{MD}}; \quad \text{Eqn (5)}$$

Equation 5, gives the magnetic field needed to maintain the ions trajectory near the ion-optical axis, where v_0 is the ions recoil velocity, Q_0 the ions charge state, B the desired magnetic field of the dipole, M_0 the mass of recoil, and R_{MD} the radius of curvature of dipole. The magnetic field needed to spatially separate ions is proportional to the ions momentum and inversely proportional to the charge state Q . Three different energy scenarios can now illustrate how the magnetic dipole separates the desired ions in terms of momentum and charge state Q . First, if the recoiling ion has momentum greater than p_0 , the ion will follow a straight line trajectory to the position of the beam dump #1, in figure 8.

Second, if the recoiling ion has momentum less than p_0 , the magnetic fields will deflect the ion in a smaller radius orbit, resulting in collision with inner wall of the deflection chamber. Third, if the recoiling ion has momentum close to p_0 , the ion will follow the intended optical path. Thus, a magnetic dipole acts as a momentum selector. Figure 9b, shows the cross-section view of the dipole with the north and south poles (electro-magnetic poles).

In figure 9a, top view of the magnetic dipole shows the trajectory of the ions as they travel through the dipole. Shields are added on the entrance and exit sides of the magnetic dipoles to reduce tumble as a result of the fringing magnetic fields (see grey area of 9b, side view). Magnetic quadrupoles labeled Q1 through Q7 in figure 8 are used to focus the ions. Quadrupoles have 4 electro-magnets with alternating north and south poles (see figure 10) that work together to focus in the x and y directions. Q1 will focus in the ions in the x-directions and the Q2 will focus the ions in the y-direction.

These quadrupole magnets in series focus ions in 2-dimensions [4]. Magnetic sextupoles of figure 11 are similar to the design of that of the quadrupole except having six poles instead of 4. Magnetic sextupoles correct for aberrations from the magnetic dipoles, resulting from things like imperfections in the design or setup of the dipoles.

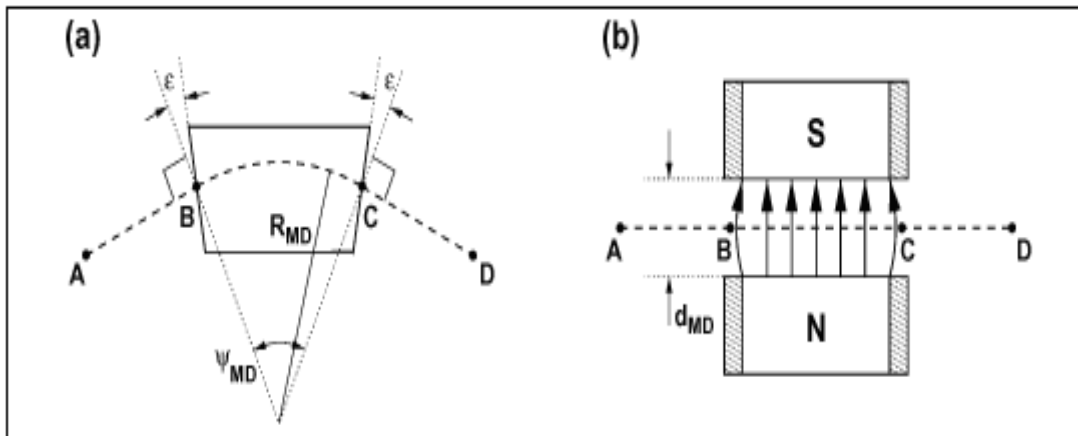


Figure 9: Figure illustrates a magnetic dipole with, (a) top view, (b) side view [4]. Arrows indicate the direction which the magnetic field points. Edges of the magnetic dipoles show some fringing of the magnetic fields in an arch at the entrance B and exit points C of b. ψ_{MD} represents the deflection angle.

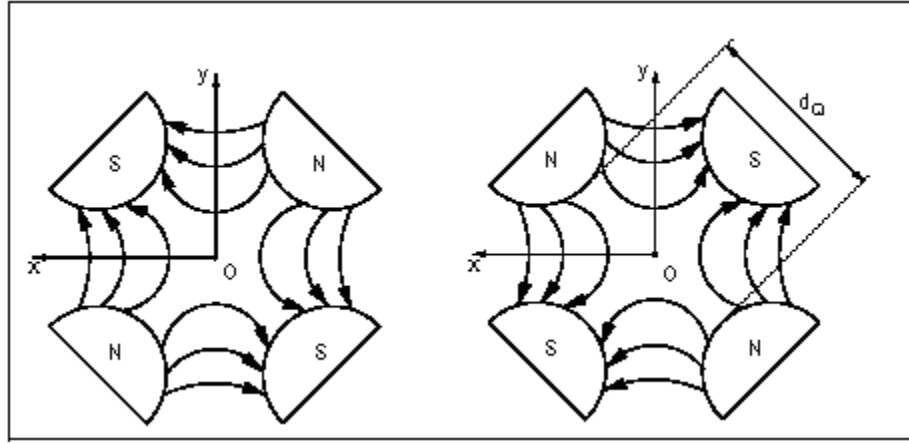


Figure 10: Magnetic quadrupoles showing the x-focusing on the left side and y-focusing on the right. The magnets are rotated by 90° between the left and right hand side. d_Q above specifies the diameter of the magnetic quadrupole [4].

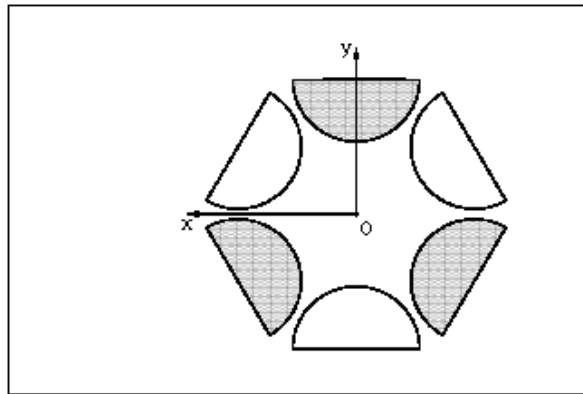


Figure 11: Magnetic sextupole showing the three sets of dipoles arranged axially [4].

The RMS has two electric dipoles in the mass separating portion. Recoiling ions of charge state Q will be attracted towards the negative dipole plate. The electric dipoles should have an electric field proportional to the total energy T_{ion} and inversely proportional to the charge as shown by:

$$QE = \frac{Mv^2}{R_{ED}} \Rightarrow E = \frac{2T_{ion}}{QR_{ED}} \quad \text{Eqn (6)}$$

E is the calibrated electric field and R_{ED} the radius of curvature. Solving for the electric field (E), results with a constant times T/Q ; the electric field is proportional to energy. Too much or too little energy will separate ions in beam dump 2 of figure 8. The ions optical axis is given in figure 12, the line AD.

The arrangement of the electric dipoles and magnetic dipoles working together is an example of a “split electric dipole mass separator”. Coupling of the E1 D3 E2 produces the mass separation portion of the RMS. No matter what distribution of energies the recoil ions have, recoil ions will be spatially sorted out at the focal plane (end point of the RMS) based on mass over charge only. The magnetic dipole is matched to the electric dipoles so that the energy dispersion produced by this dipole counteracts the energy dispersion of the electric dipoles. Equation 7 gives the mass to charge ratio of ions tuned through the split mass separator where r = radius of curvature, B = magnetic field, and E = electric field.

$$A/Q = rB^2/E \quad \text{Eqn(7)}$$

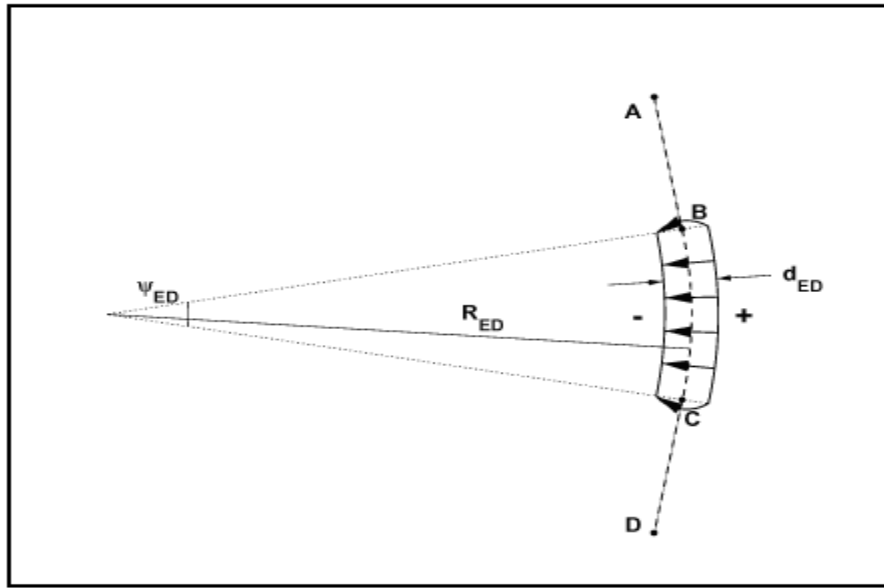


Figure 12: Schematic of electric dipole showing + and – plates with ions trajectory A to D [4]. Electrostatic dipole plates are bent to compensate for the ions trajectory. R_{ED} is the radius of curvature and d_{ED} is the distance between the plates of the dipole. Ψ_{ED} is the deflection angle, large deflection angles require curved plates.

Chapter 4: Fusion Evaporation Cross-Section

4.1 *Introduction to HIVAP Production Code*

In planning an experiment one needs to know the beam energy, beam current, and what species of beam and target are best suited for the desired studies. The cross-section for the desired ion to be produced depends on the beam energy. The beam current required is dependent on the cross-sections of the desired product, which in turn depends on the species of projectile and target used. The questions of what beam energy, what beam current and what species should be used in an experiment may be determined by good knowledge of the cross-sections. In order to predict production cross-sections, computer codes that use the statistical model of nuclear fusion reactions are used.

For a given combination of target and projectile nuclei, the HIVAP [12,13,14,15,16] code can be used to calculate the production cross sections of nuclei produced in a fusion-evaporation process at any given beam energy.

The nuclear reaction model used for HIVAP calculations separates the process into two stages. The first is the formation of the compound nucleus in a central collision of the beam and target nuclei; the second is the statistical process of evaporation of nucleons, alpha particles, and gamma rays, which carry away the excess energy from the compound nucleus. It is the second process which determines the relative cross-sections for nuclei which can be produced in a given reaction.

Production cross-sections in the vicinity of ^{100}Sn near the α island, see figure 2, have been estimated with the HIVAP statistical code. Simple kinematics considerations

allow transformation of cross section calculations made for the so called “normal kinematics” (^{54}Fe beam on ^{58}Ni , *this experiment*) into the “reverse kinematics” situation (^{58}Ni beam on ^{54}Fe , *opposite reaction such as HIVAP*). Both of these situations have been exploited experimentally.

HIVAP parameters such as the level densities are modeled in relation to excitation energies; as excitation energy increases so does the number of levels. The probability of evaporation also depends on the number of levels available and the spin of each level.

Other parameters such as competition with various particle evaporation channels are estimated for evaporation of protons, neutrons, and alpha particles. The code used experimental binding energy data to estimate how many particles are emitted from a given compound nucleus with a given excitation energy.

For charged particles the coulomb barrier transmission coefficient $T_l(E)$ must be calculated. Transmission coefficients for penetrating waves, such as evaporation of protons and alpha particles are calculated [17]:

$$T_l(E) = \{1 + \exp(2\pi(B_l - E)/\hbar\omega_l)\}^{-1} \quad \text{Eqn (8)}$$

Where ℓ is the angular momentum of the wave penetrating the coulomb barrier. B_l is the barrier height, and $\hbar\omega_l$ represents the curvature of the harmonic oscillator potential (inverted). Many other parameters are also required in the code. Some other parameters may involve phenomenological approaches.

Input parameters for HIVAP are the available excitation energy delivered from the beam. The excitation energy must first be calculated to use HIVAP output. HIVAP gives output similar to a table, where the excitation energies are given on a vertical scale

and the species are given on a horizontal scale. In order to find the cross-section, one would calculate the excitation energy first and find the desired species to be produced.

First, the center of mass energy will be estimated. This reaction is inelastic; in the center of mass system, the collision energy is converted into excitation of the nucleus.

Total energy of the primary beam is measured in the lab frame E_{Lab} and will be transformed to excitation energy of the recoils products, and energy is carried off as kinetic energy of recoiling products, the rest. The center of mass energy is given by:

$$E_{c.m.} = \frac{m_2}{m_1 + m_2} E_{lab}; \quad \text{Eqn (9)}$$

Where m_2 = mass of the target nickel; and m_1 = mass of projectile iron. Laboratory frame energy is the energy of the accelerated primary beam. Second, an estimate of the energy needed for fusion will be needed. Using mass tables from [18] the Q value or reaction energy can be calculated with M_{58} = target, M_{54} = projectile, and M_{112} compound nucleus:

$$[(M_{58} + M_{54}) - M_{112}]C^2 = Q; \quad \text{Eqn (10)}$$

M_{112} represents the mass of the fused compound nucleus. The Q value can be calculated from the mass difference ΔM between the sum of target and projectile masses and mass of the compound nucleus. One can deduce the available energy for excitation of the xenon nucleus as the sum of the center of mass energy and the reaction energy:

$$E^* = E_{c.m.} + Q; \quad \text{Eqn (11)}$$

Third, excitation energy can now be used as input for HIVAP data to find cross-sections for all A=109 isobars. The output cross-section predictions of HIVAP are in units of millibarns.

4.2 *HIVAP and Apparatus Tuning*

The primary beam energy from the tandem is an important parameter for exotic ions. The cross-sections for production of exotic nuclei are sensitive to the primary beam energy. To maximize production of the desired nucleus in a reaction, proper choice of the primary beam energy is essential. The HIVAP code can serve as a tool for estimating the beam energy to maximize the desired ions. The production cross-section for a given nucleus as a function of energy, called the excitation function, is a monotonic function with one or more local maxima and dropping to zero for energies which are too large or too small. The HIVAP code provides the experimentalist with an estimate of the energy for maximizing the production cross section. The physics behind the shape of the excitation function is determined by two phenomena, tunneling through the Coulomb barrier in the fusion process and statistical de-excitation of the nucleus.

Excessively high beam energies will produce high excitation energy in the ^{112}Xe nucleus, resulting in evaporation of more protons and neutrons (figure 13), and thus producing nuclei with smaller mass than the desired nucleus.

On the other hand if the primary beam energy is too low, $E < 180$ MeV (see figure 13), the projectile ^{54}Fe ions cannot penetrate the ^{58}Ni Coulomb barrier to form the compound nucleus ^{112}Xe . As seen in figure 13 the cross-section for production of ^{109}I vanishes below ~ 180 MeV; because the fusion process cannot occur.

The ideal beam energy to maximize production of ^{109}I ions is around 200 to 210 MeV. The compound nucleus ^{112}Xe was excited to a level favoring the production of ^{109}I by evaporating 2 neutrons and 1 proton.

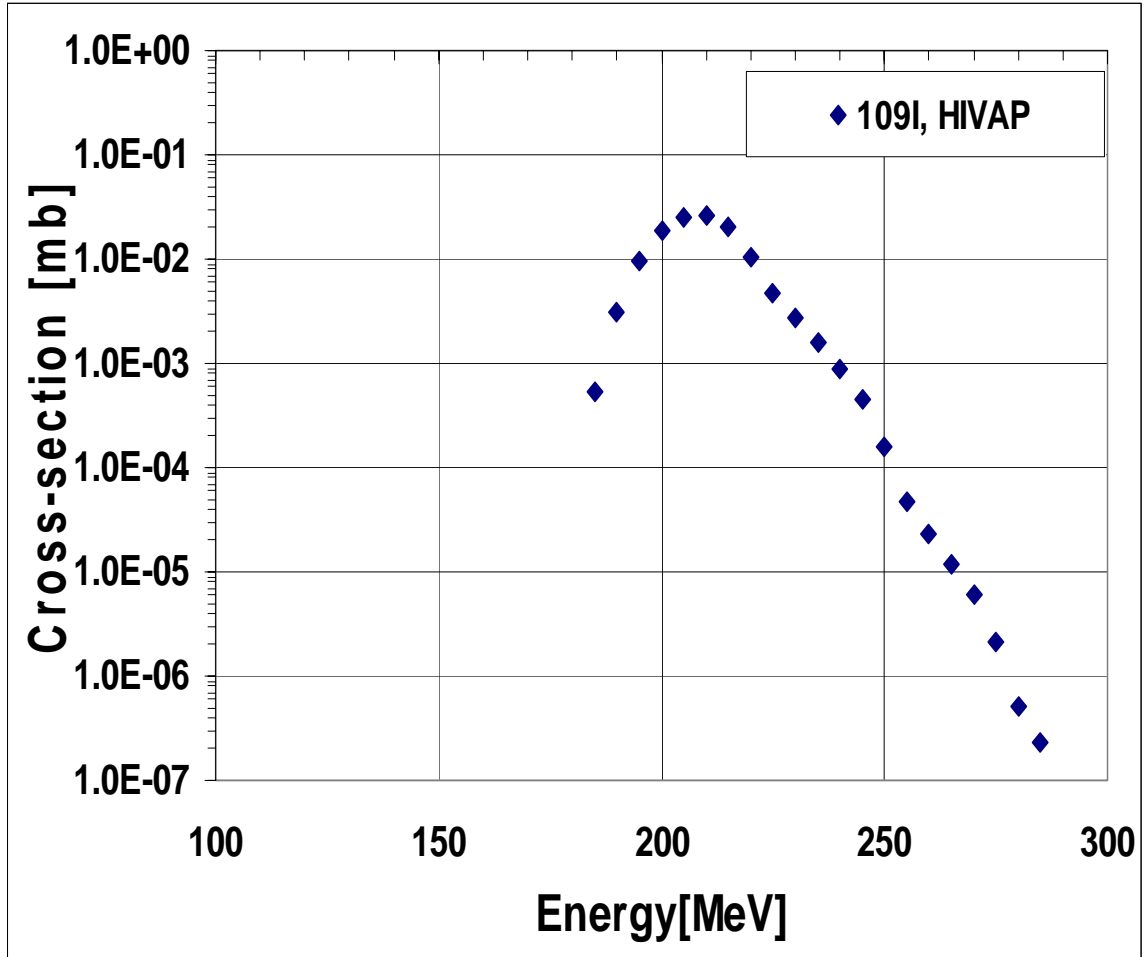


Figure 13: Cross-section data from HIVAP showing the prediction of the cross-section for ^{109}I . Three areas of the figure are of interest. The energy for three cases are illustrated as being below 180 MeV, where the fusion process has not occurred and beam energy above 285 MeV where production of smaller mass products other than iodine has become dominant. Beam energies of 200-210 MeV maximize production of ^{109}I [19].

Calculations using the fusion-evaporation code HIVAP were used to compare with this experiment. In order to compare with the experimental production rates, one has to first convert from HIVAP into production rates. The unit scales have to match, where the experimental rates have been estimated in cross-sections (mb) to compare with HIVAP's predictions. The reaction rate (measured ions) or yield of ions produced at the target is given by

$$R = \sigma IN \quad \text{Eqn(12)}$$

where sigma is the cross-section to be calculated, I represents the incoming beam current from the tandem accelerator, and R represents the detected ions produced from detectors. The number of ions available at the surface of the target N can be expressed as the following:

$$N = (\rho N_A) / A$$

In this expression ρ represents the thickness of the target in grams per unit area, N_A is Avogadro's number, and A is the molecular weight of the target material. Equation 12 can be rearranged to give the cross-section in terms of the count rates from experimental data as

$$\sigma = R / (\epsilon_{\text{RMS}} \text{ efficiency} * I * N) \quad \text{Eqn(13)}$$

where R represents the implantation rate at the DSSD.

The production cross-sections of A=109 isobars as predicted by HIVAP are listed in table 2. The cross-sections from HIVAP data decreases by a factor of 5 from ^{109}Sb (9.43×10^{-2}) to ^{109}Xe (1.33×10^{-7} b); as one moves further away from the line of stability an

intense beam current is needed in order to produce ^{109}Xe , which is produced with a cross-section of $\sim 10^{-4}$ mb (see table 2).

Caution must be exercised in comparing rates to HIVAP as mentioned in chapter 4. Differences in the parameterizations can make results of the code questionable and comparisons to experimental data have to be applied.

In this experiment two spectroscopic techniques were used to measure production rates. The first method used charged particle decay to estimate the total rate of ions. The second technique used gamma-ray production to estimate the total counts of ions. A high-purity germanium detector was used to detect gamma rays from the implanted radioactive isotopes, and a charged particle silicon detector was also used to detect alpha particles and the total number of separated ions implanted into the DSSD. Gamma rays had very little interaction with the silicon material because the silicon material is thin (65 μm). Charged particle decays such as protons or alphas have a short range in material in comparison to gammas, making them much more efficient to study.

Table 2: HIVAP output, for A=109 isobars measured from this experiment. Ion implanted on the DSSD is given in column one along with the proton number in column 2. Out put from HIVAP is given in column three, cross sections in millibarns (mb).

Ion Produced	Proton #, Z	Cross-Section,(mb)
^{109}Xe	54	1.33E-04
^{109}I	53	1.48E-02
^{109}Te	52	1.21E+01
^{109}Sb	51	9.43E+01

The result of interaction of charged particles or gamma rays with detector material is the release of charge carriers in the semiconductor detector that are collected and form an electronic signal. In both methods, one has to know the efficiency for detecting the respective decay rates and hence, calibration of the detectors is required.

Chapter 5: Detector Apparatus

5.1 Calibrating a Germanium (Gamma Detector)

The 40% hyper-pure germanium detector was calibrated with a well known source containing a mixture of isotopes, ^{154}Eu , ^{125}Sb , and ^{155}Eu from the National Institute of Standards and Technology 4275C [NIST]. It is a point source in a polyester tape.

The activity and energies of the gammas being emitted from the point source are known. The source was placed approximately 6 cm in front of the germanium detector and counts were taken for 2072 seconds. The energy calibration yielded the straight line in figure 14, which was fitted with the equation:

$$\text{Channel} = 6.1388E - 1.6726 \quad \text{Eqn(14)}$$

For any other experiments, the same calibration, eqn(14), can be used to obtain the energy of any gamma that enters the germanium crystal. Once the energy calibration is accomplished, the efficiency calibration can be performed, using known source strength. The source was calibrated on September 1, 1988, and hence, the current activity for May 21 2007 must be calculated. The time elapsed was 5.90×10^8 seconds, and the activity of each gamma ray from the source in gammas/second $R(t)$ can be estimated from the equation 15 where λ is the decay constant of the activity:

$$R(t) = R_0 \exp(-\lambda t) \quad \text{Eqn (15)}$$

The product of $R(t)$ and sample measurement time (2072 seconds) gives the total expected counts. The decay constants for this source were $7.96 \times 10^{-9} \text{ sec}^{-1}$, 4.62×10^{-9}

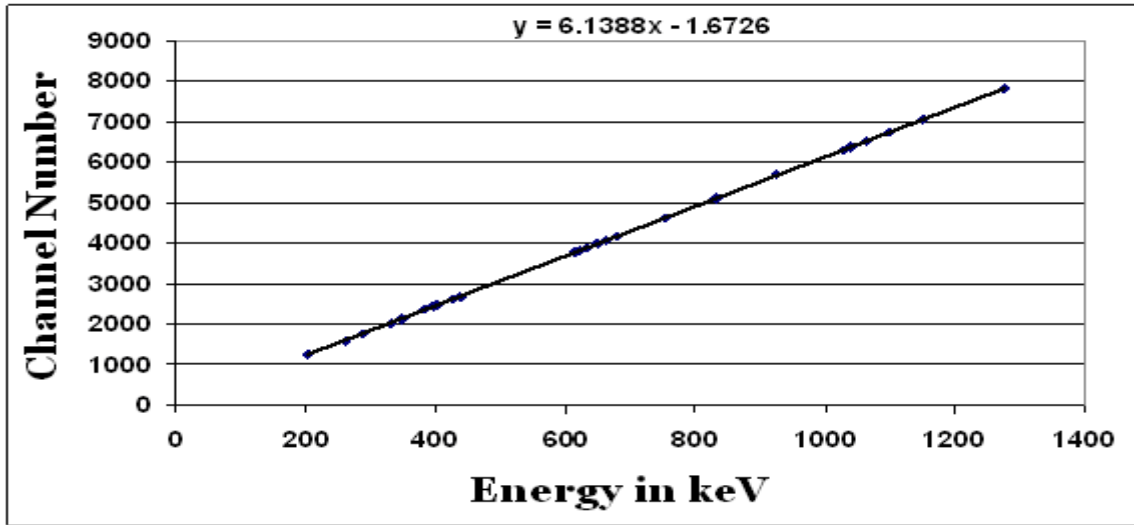


Figure 14: Germanium energy calibration showing relationship between channel number on vertical scale and energy on horizontal scale. Linear regression gives the best fit calibration of this detector with a sensitivity of 6.1388 channel per keV.

sec^{-1} , and $2.55 \times 10^{-9} \text{ sec}^{-1}$ for ^{125}Sb , ^{155}Eu , and ^{154}Eu nuclides in this sample. The detection efficiency was measured by obtaining the number of gammas counted in 2072 seconds and dividing by $R(t) \times 2072$ the total gammas emitted by the source. Efficiency is a measure of the counts to the total expected counts. A linear regression fit of the efficiencies as a function of energy for the germanium detector on a log-log scale is shown in figure 15. Linear regression gives the following equation with constants, $B = 1.3285$ and $A = -0.9119$.

$$\text{Log}(\epsilon) = A \text{Log}(E) + B \quad \text{Eqn (16)}$$

The energies and detection efficiencies for a particular photo peaks belonging to ^{109}Te and ^{109}Sb , selected to calculate the number of recoil ions emitting these gammas are listed in table 3. The ion emitting the gamma ray, its energy, channel number and its efficiency are displayed. The far right column of table 3, indicates if any contaminations of

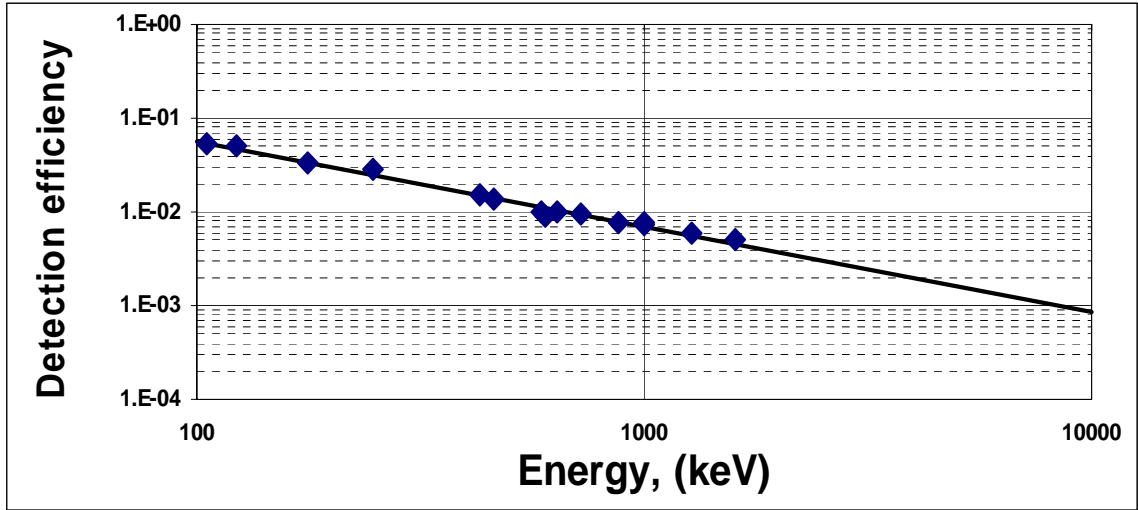


Figure 15: Log-log plot of germanium detection efficiency to energy. Result is a fit to a straight line, where the line is used to guide the eye, the efficiency, not shown, will drop below 130 keV. A straight line fit (above 130 keV) is in a good agreement with experimental points.

multiple photo peaks sharing the same energy occur, like 832 keV from ^{109}Te and 832.58 keV from ^{105}In .

The elimination of peaks that were possibly contaminated lead to only a few good peaks, free of contamination, 402, 1061.8, 925 keV as listed on table 3 highlighted in yellow. Estimation of ions that decay by gamma emission is given as:

$$\text{Ions} = \frac{I_{\text{exp. counts}}}{\varepsilon * br} \quad \text{Eqn (17)}$$

where ions is the number of implanted recoil ions responsible for the gammas emitted, (I_{exp}) is the number of gamma counts collected with the calibrated Germanium detector, (ε) is the efficiency and (br) is the branching ratio of the photo-peak. Of the highlighted ions in table three, only the 402 keV transition was used to estimated counts for this experiment because the photo peak has no other gamma ray matching it and this peak has

Table 3: Photo peaks taken from ^{109}Te and ^{109}Sb data collected from the calibrated germanium detector. Ions responsible for the peaks in column one, column two lists the photo-peaks energy, column three lists the channel number where the photo-peak is expected to be. The counting efficiency are given in column four and comments about contaminated peaks on far right.

Peaks	Energy	Channel	Efficiency	Comments
^{109}Te	402	2467.1	0.015928	No contamination
^{109}Te	752	4163.7	0.008998	Contamination
^{109}Te	831.6	5105.6	0.008209	Contamination
^{109}Te	1274.1	7819.6	0.005563	Contamination
^{109}Sb	260.8	1599.3	0.023634	No contamination
^{109}Sb	664.2	4077.1	0.010076	Contamination
^{109}Sb	678.3	4163.7	0.009885	Contamination
^{109}Sb	925	5678.2	0.00745	No contamination
^{109}Sb	1061.8	6515	0.006569	No contamination
^{109}Sb	1496.1	9181.4	0.004805	No contamination

a large number of counts. A full energetic spectrum of the gammas collected is given in figure 16. Some ions implanted into the DSSD may not decay by emitting gammas, but instead may decay by charged particle decay, such as alpha decay .

5.2 Alpha Counts from Silicon Detector

Alpha decays can be counted with a silicon detector. The recoil ions I, Te, and Xe decay by charged particle emission. The incident ions have a 20% energy spread, where the maximum energy implanted onto the DSSD is 60 MeV. The spread in energy results in ions implanted at different depths in the DSSD. An alphas emitted by ions implanted near the front surface has a chance of escaping the detector without depositing its full energy and such an escaping alpha will not be counted. The efficiency of the silicon detector can therefore have a range from 70% to 100%. It has been estimated that ion implantation energy of 60 MeV or more will result in an efficiency of nearly 100%. For example, 60 MeV ^{109}Te ions have a range of 13 μm which is larger than the alpha

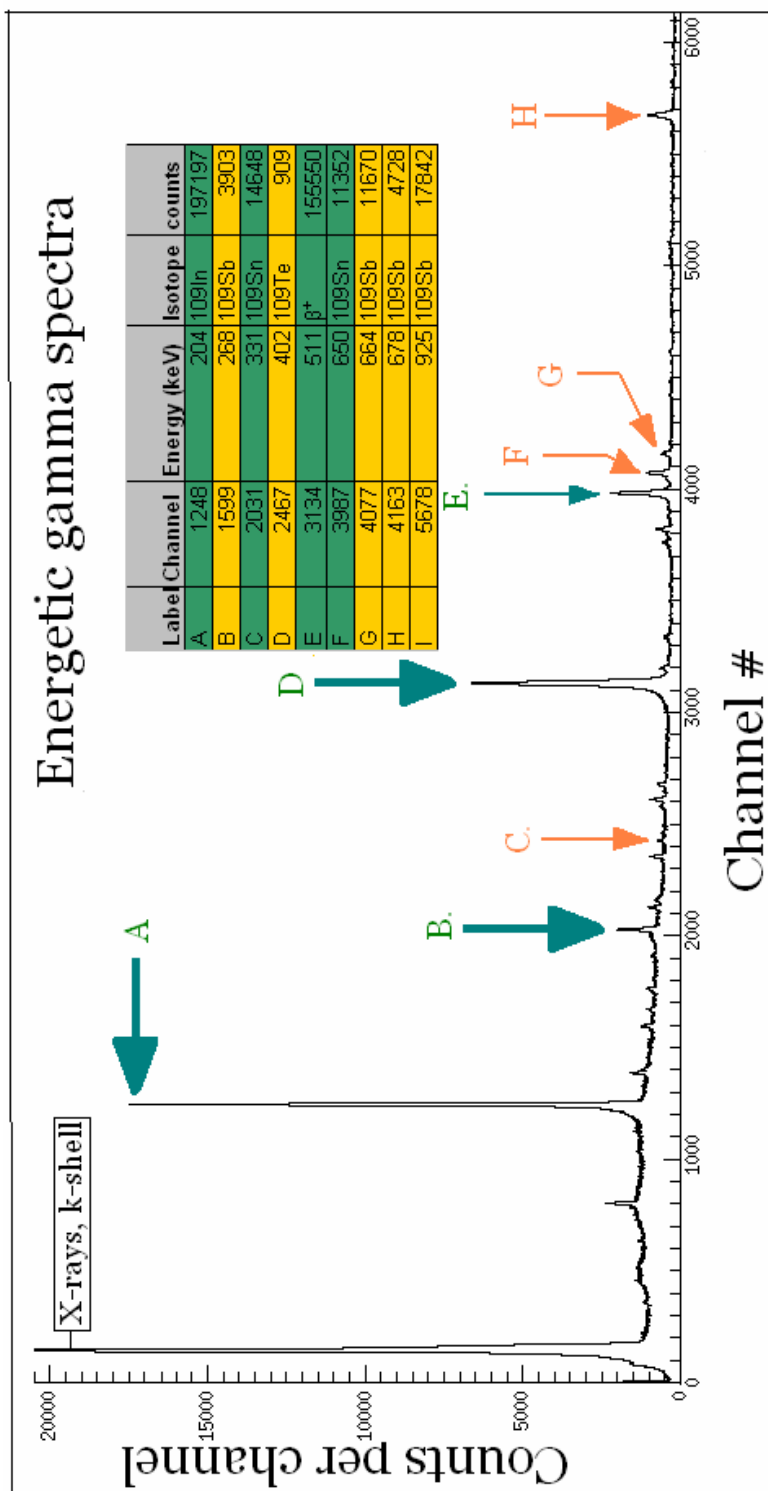


Figure 16: Energetic gamma spectra showing some of the most intense peaks from the gamma collected from the germanium detector. One of the most clearest peaks is the 402 keV line.

range of 12 μ m for 3.08 MeV alpha particles. Thus, for implantation energy of 60 MeV, the overall efficiency will likely be 100%. However, for lower implantation energies, some of the alphas may escape, resulting in a smaller efficiency for detecting alphas. The number of implanted ions can then be deduced:

$$\text{Ions} = \frac{I_{\text{exp. counts}}}{br} \quad \text{Eqn (18)}$$

Parameters are the same as equation 17, and it is assumed that $\epsilon = 1.00$. Table 4 gives the production rates in counts/minute for the 4 decays, 2 alphas and 2 gammas that span a proton range of 51 to 53. Theoretical rates are at the far right of the table 4 for comparison.

Table 4: Ion production rates of A=109 isobars in comparison to HIVAP's prediction. Comparisons are based on a count rate, number of ions counted per minute.

Decay	Ion	Proton #	Branching Ratio %, br	Efficiency %, ϵ	ions/(sec.)	Meas. Cross-sec.	HIVAP cross-section (mb)
Alpha	I	53	49	70-100	1.05E+00	2.68E-02	1.48E-02
Alpha	Te	52	3.9	70-100	1.67E+02	4.28E+00	1.21E+01
Alpha	Xe	54	100	70-100	2.83E-04	7.28E-06	1.33E-04
Gamma	Te	52	13.1	1.59	1.40E+02	3.60E+00	1.21E+01
Gamma	Sb	51	17	0.65	2.81E+03	7.22E+01	9.43E+01

Chapter 6: Discussion of Results

The aim of this experiment was to measure production cross-sections for exotic nuclei near ^{100}Sn and compare the data with the predictions of the fusion evaporation code HIVAP. These tests are important in order to assess the applicability of the code to estimate unknown cross sections.

The drop in production rates for ^{109}Xe and ^{109}I is a result of the particle evaporation from the compound nucleus ^{112}Xe . An example of the intensities of each evaporation process is given in figure 17. The cross-section is listed for each nucleus produced from HIVAP and the arrows represent the intensities for each particle in the evaporation process. Protons will dissipate less of the excitation energy each time a proton is evaporated, and more protons can therefore be evaporated leading to higher productions for ^{109}Sb and ^{109}Te . For proton rich nuclei neutron evaporation requires the most energy. With a given amount of excitation energy, E^* , neutrons will carry off more energy per particle leading to less production of ions that require the neutron evaporation channel, like ^{109}Xe and ^{109}I .

In order to determine production cross section for beta decaying ^{109}Sb , gamma radiation data has to be verified against alpha decay data for consistency. Normalization of data from alphas and gammas for ^{109}Te is based of measured decay data using equations 16 & 17. The number of ^{109}Te atoms collected in the DSSD during the experiment was determined by counting alpha particles and independently by counting gamma rays assigned to ^{109}Te decay. Since both methods count the same number, the results of the two measurements should be the same. However, the number of ions implanted

implanted was measured with gammas as estimated to be 140 ions/sec from charged particle decay the number of implanted ions was estimated to be 167 ions/sec (from table 4). The ratio of the counts estimated from gammas to counts estimated from alphas is 84 %. A normalization factor was then used for the gamma counts to give agreement with counts from the alpha decays. The gamma counts were normalized instead of normalizing the alpha counts. The alpha detection used here was more accurate than the gamma detection. One reason is the alpha detector had a full 4π solid angle of detection in comparison to the germanium detectors intercepting a small fraction of the full solid angle. Uncertainties in gamma detection may be due to calibration from a point source from ^{154}Eu , where the actual gammas detected from the nuclei implanted in the DSSD has a shape of a disc. In order for the counts from the gammas to match the counts from alphas for tellurium, the gamma data were multiplied by 1.19. This normalization was applied to all gamma decay data measured.

Experimental data from ^{109}Te was also normalized with the predictions from HIVAP since the HIVAP has been shown to predict well the cross-section for the production of this isotope [19]. The need for normalization is perhaps due to uncertainties in estimating the RMS transmission efficiency and a poor estimate of the primary beam intensity.

Experimental data collected gave 167 counts/sec or 4.28 millibarns for production of ^{109}Te versus the HIVAP prediction of 12.1 millibarns. A normalization factor of ($\sim 12.1/4.28$) 2.83 for the experimental data brought it into agreement with the HIVAP predictions for ^{109}Te . All other data points (experimental) were also shifted by the same factor.

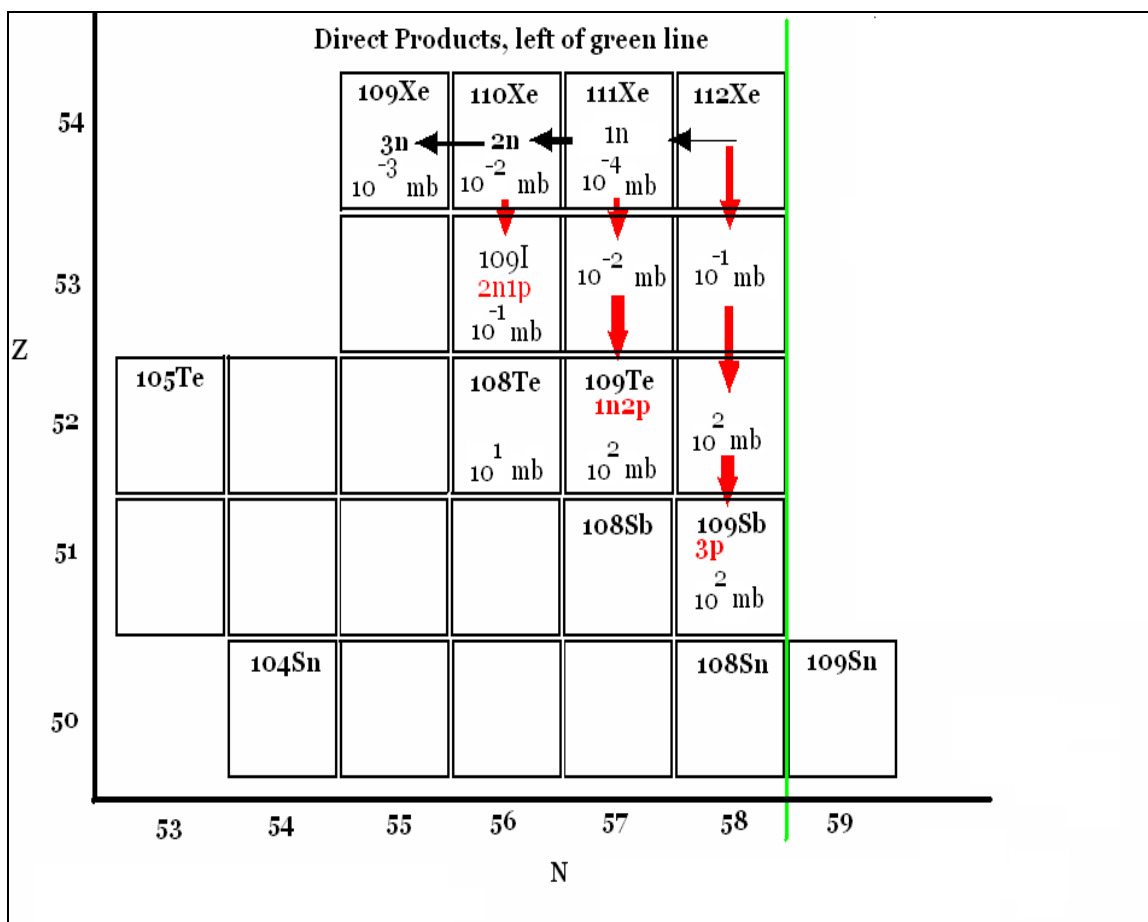


Figure 17: Evaporation channels leading to ^{109}Xe , ^{109}I , ^{109}Te , and ^{109}Sb . The cross-sections for the tellurium and antimony are much higher in comparison to xenon and iodine. Red arrows indicate proton evaporation and black arrows neutron evaporation.

In figure 18, the cross-sections from HIVAP, gamma detection method, and charged particle detection method are plotted. In comparison with the cross-section of tellurium, HIVAP underestimates experimental data for I($Z = 53$) and overestimates data for Xe($Z = 54$) after the normalization procedure. Xenon so far has the largest disagreement, approximately one order of magnitude difference between experimental data and HIVAP.

According to figure 18, a rapid drop off is measured at $Z = 53$ iodine production. Recall that the compound nucleus having high excitation energy will attempt to cool down by proton, neutron, or alpha evaporation. Since the proton has lower separation energy in relation to the neutron separation energy, the proton evaporation channel is the dominating channel for evaporation. This leads to the large production of ions from the $3p$ and $1n2p$ channels and much smaller production from the $2n1p$ and $3n$ channels. The differences in the jump may be a good example of where the caution given earlier comes in. These nuclei in the vicinity of Alpha Island have very small proton binding energies. Theoretically a large jump between $2n1p$ (^{109}I) and $1n2p$ (^{109}Te , see figure 18) is expected. Experimental data does suggest a difference in the cross-section of ions formed from the $2p1n$ and the $1p2n$ evaporative channels, but experiment cross-section does not drop by 3 orders of magnitude predicted by HIVAP. The experimentally measured ion production cross-section drops by 2 orders of magnitude between $Z=52$ and $Z=53$. The results obtained are consistent with the previous results obtained by Korgul [19], who measured the production cross-section for Xe, I, and Te as a function of primary beam energy. The experiment presented in this thesis extends Korgul's data by

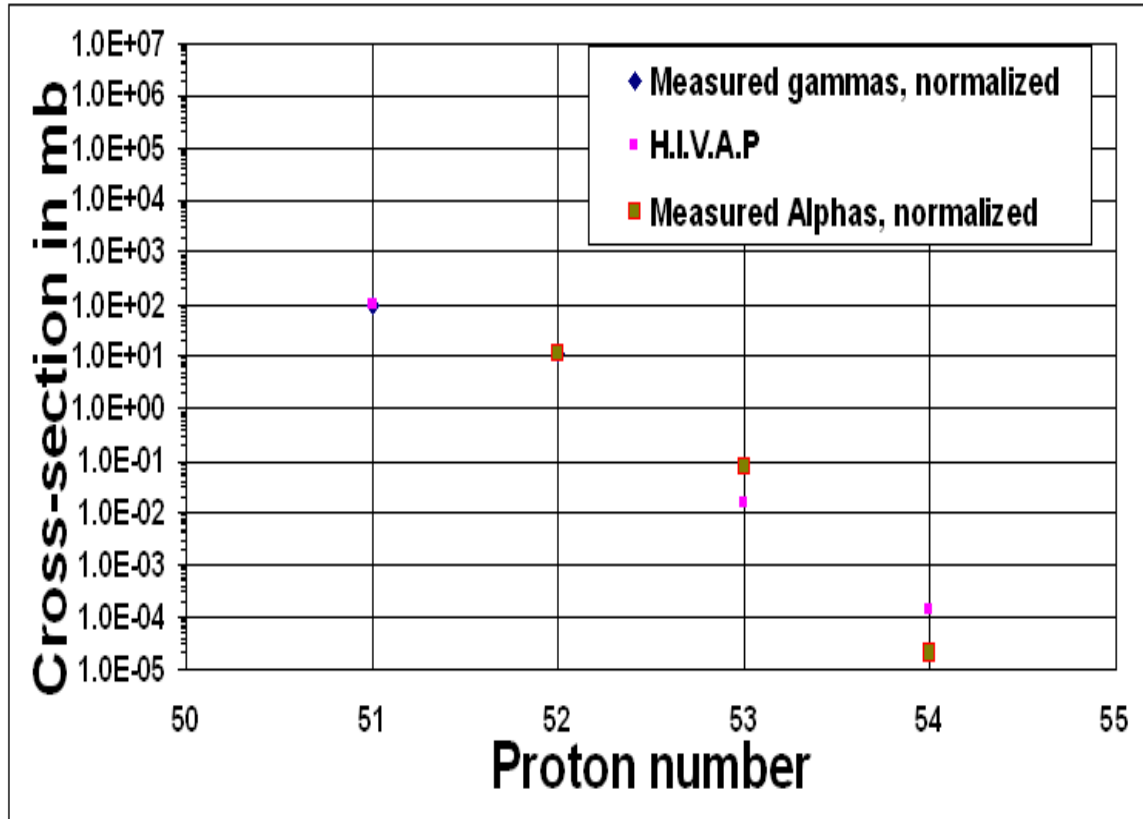


Figure 18: Experimental production rates for ^{109}Sb for $Z=51$, ^{109}Te for $Z=52$, ^{109}I for $Z=53$, and ^{109}Xe for $Z=54$ in comparisons with HIVAP predictions. All data points are normalized for $Z=52$.

does not drop by 3 orders of magnitude predicted by HIVAP. The experimentally measured ion production cross-section drops by 2 orders of magnitude between $Z=52$ and $Z=53$. The results obtained are consistent with the previous results obtained by Korgul [19] & see figure 19, who measured the production cross-section for Xe, I, and Te as a function of primary beam energy. The experiment presented in this thesis extends Korgul's data by adding another point for ^{109}Sb . The results of this experiment agree with Korgul's experimental results for ^{109}Xe , ^{109}I , and ^{109}Te for overproduction of experimental counts for ^{109}I and underproduction of experimental counts for ^{109}Xe (see figure 19). Tellurium production cross-section data and HIVAP's prediction data both agree with Korgul's results.

The disagreements presented between experimental findings as well as Korgul's data and HIVAP data are not certain. This disagreement might be due to transmission efficiencies for each isotope that may vary due to the charge state distribution transmitted through the RMS.

In conclusion, production cross-section of $A=109$ isobars produced in the fusion of ^{54}Fe with ^{58}Ni were compared with HIVAP calculations. HIVAP predicts the production cross-section of ^{109}Sb fairly well, but underestimates ^{109}I (2n1p channel) and dramatically overestimates the ^{109}Xe (3n channel). The disagreements may be due to the parameterizations that HIVAP uses or due to transmission efficiency through the Recoil Mass Spectrometer caused by variations in ionic charge state distribution. Further systematic experiments in this region of alpha activity coupled with parameter tuning predictions are required in order to understand the observed discrepancies.

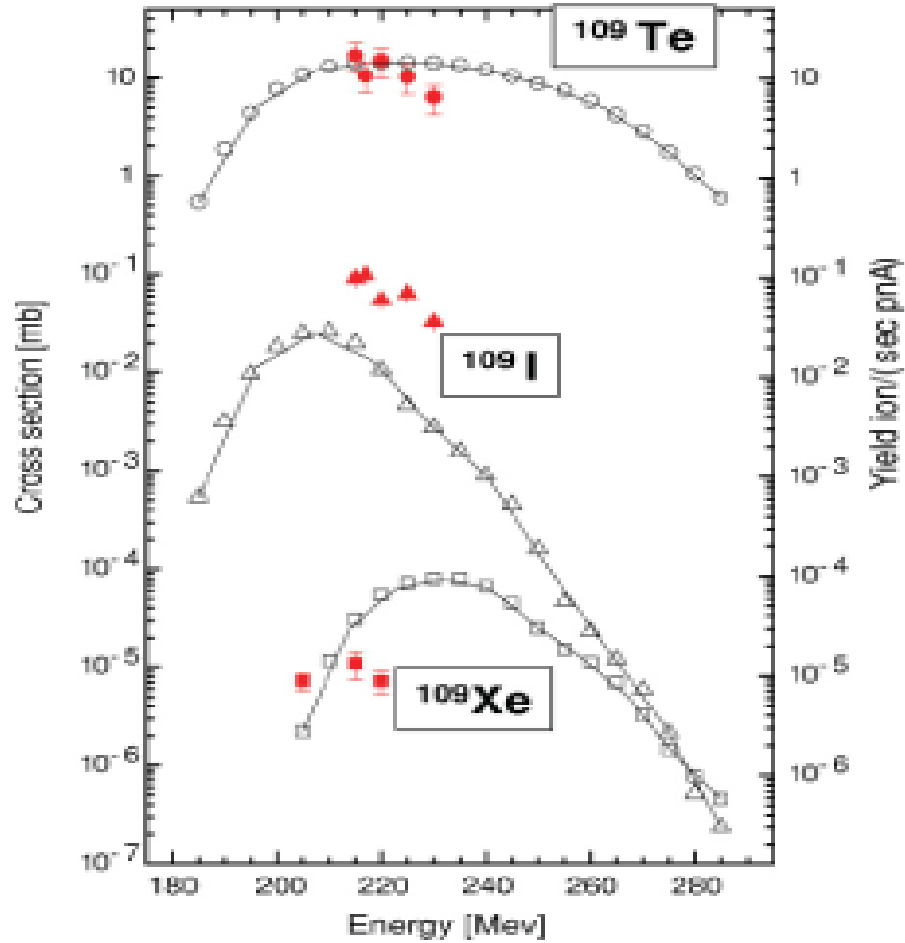


Figure 19: Cross-section in mb versus the energy for excitation functions of various products separated from the RMS. Hollow squares, hollow triangles, and hollow circles are HIVAP's predictions. Data marked in red is experimental data from Korgul et al. [19]. Experimental data is lower for production of ^{109}Xe and higher for production of ^{109}I , but the data agrees with HIVAP for ^{109}Te .

Bibliography:

- [1] H.Schatz et al. Phys. Rev. Lett. **86**, 3471 (2001).
- [2] S.N. Liddick et al. Phys. Rev. Lett. **97**, 082501 (2006)
- [3] R.D. Mac-Farlane et al. Phys. Rev. Lett. **14**, 114 (1965)
- [4] Thomas Nelson Ginter, The New HRIBF Recoil Mass Spectrometer Performance and First Results, Dec. 1999, Ph.D Thesis, Vanderbilt University
- [5] Mazzocchi et al. Phys. Rev. Lett. **98**, 212501, (2007).
- [6] V.A, Karnaukhov et al. Soviet J. Nucl. Phys. **4**, 327 (1967)
- [7] E. Roeckl et al. Nucl. Phys. **A326**, 65-82 (1979)
- [8] Z. Dombardi et al. Phys. Rev. C **51**, 2394 (1994).
- [9] J. J. Ressler et al. Phys. Rev. C **66**, 024308, (2002).
- [10] <http://www.pelletron.com/pellet.htm>
- [11] <http://www.phy.ornl.gov/hribf/accelerator/fac-layout-hptl.shtml>
- [12] W. Reisdorf et al. Z. Phys. **A 300**, (1981) 227.
- [13] W. Reisdorf et al. Z. Phys. **A 343** (1992) 47.
- [14] Andreyev A N et al. Nucl. Phys; **A 626** 857 (1997).
- [15] Veselsky M et al. Z. Phys; **A 356** 403 (1997).
- [16] W. Reisdorf et al. Nucl. Phys. **A 444** (1985) 154.
- [17] A.N. Andreyev et al. Phys. Rev, **C 72**, 014612 (2005).
- [18] G. Audi et al. Nucl. Phys, **A 729**, 337 (2003) “Mass Tables”
- [19] A. Korgul et al. Phys. Rev, **C 77**, 034301 (2008).

Vita:

Elton Lewis Freeman graduated from Pepperell High School in May of 1994. He then attended a community college at Floyd College in Rome Georgia. He later moved to the State University of West Georgia, and obtained his B.S. degree. In graduating from “West Georgia”, he was awarded the Who’s Who award and was awarded the Georgia Academy of Science Best Presenter award in a year before graduation for his talk on “RC Circuits”. He also gave talks at the Georgia Academy of Science during his graduation on “Alpha Particle Decay” and “Does the Alpha Particle Really Exist within the Nucleus”.

Upon entering the University of Tennessee, he was interested in the field of nuclear physics and decided to do research in relation to low energy nuclear physics, a carry over from his undergraduate work from UWG. In graduating from UTK, he Accepted membership of the Sigma Pi Sigma honor society in physics, and he is still currently a member of the Society of Physics Students (SPS) and a member of the American Association of Physics Teachers. He has really enjoyed teaching his engineering students 231 and 232 labs as a teaching assistant. He has also been awarded the outstanding teaching assistant award by the American Association of Physics Teachers (AAPT) in 2007-2008.

Elton obtained his Master’s of Physics Degree from University of Tennessee in the summer semester of 2008. His future plans of course are to continue his studies.